Slip kinematics and dynamics during and after the 1995 October 9 $M_w = 8.0$ Colima–Jalisco earthquake, Mexico, from GPS geodetic constraints

W. Hutton,[1,*] C. DeMets,[1] O. Sánchez,[2] G. Suárez[2] and J. Stock[3]

[1] *Department of Geology and Geophysics, University of Wisconsin-Madison, Madison, WI 53706 USA*
[2] *Instituto de Geofísica, UNAM, México D. F., México*
[3] *Seismological Laboratory, California Institute of Technology, Pasadena, CA 99125 USA*

SUMMARY

We use horizontal and vertical crustal displacements derived from GPS measurements at 26 sites in western Mexico to study the coseismic and post-seismic kinematics and dynamics of the 1995 October 9 ($M_w = 8.0$) Colima–Jalisco earthquake along the Middle America Trench. The measurements bracket the entire landward edge of the approximately 150 km long rupture zone and span a 4 yr period for most sites. We solve for the temporal evolution of slip along the subduction interface by inverting GPS displacements for the coseismic and four post-seismic intervals (March 1995–March 1999), subject to the assumption that the crust responds elastically to slip along a shallow-dipping, curved subduction interface. Coseismic rupture of up to 5 m was largely focused above depths of 20 km and was limited to a 120–140 km long segment of the subduction zone. Within one week of the earthquake, post-seismic slip migrated downdip to depths of 16–35 km, where it has since decayed logarithmically. We also find evidence for shallow aseismic slip during 1996 or early 1997 northwest of the coseismic rupture zone and increasingly widespread relocking of shallow regions of the subduction interface after early 1997. The relative lack of afterslip in shallow regions of the subduction interface suggests that the interface lies in the unstable frictional regime and hence is strongly coupled between earthquakes. By 1999, the cumulative slip moment associated with post-seismic slip equaled ~ 70 per cent of the coseismic moment, with nearly all of this slip occurring downdip from the coseismic rupture zone. The migration of slip after the earthquake to a deeper and presumably velocity-strengthening area of the subduction interface and the logarithmic decay of afterslip conform to the qualitative and quantitative predictions of a model in which the fault kinematics are prescribed by rate- and state-variable frictional laws. However, misfits to the geodetic displacements exceed the average displacement uncertainties for all epochs, implying one or more of the following: (1) the elastic response is heterogeneous due to slip along unmodelled upper crustal faults or variations in the elastic properties of the crust; (2) other post-seismic mechanisms such as viscoelastic or poroelastic effects contribute to or possibly dominate the post-seismic response; (3) we have underestimated the uncertainties in the GPS displacements.

Key words: crustal deformation, earthquakes, fault slip, geodesy, subduction, tectonics.

1 INTRODUCTION

Over the past century, seismologic studies of large subduction zone earthquakes have yielded a wide range of useful information about the kinematics and dynamics of slip along sub-

duction faults. Significantly less is known about the dynamics of subduction during the post-seismic and interseismic phases of the subduction seismic cycle since seismometers cannot measure displacements that occur over periods longer than ~ 1 day and because geodetic instruments that can measure such displacements have only rarely been located close enough to major subduction earthquakes to yield useful constraints on the kinematics

* Now at: Instituto de Geofísica, UNAM, México D. F., México

of slip along the subduction interface. More information about crustal movements during the interseismic and transient post-seismic phases of the seismic cycle is needed to better understand whether and how aseismic processes accommodate plate convergence during these phases of the seismic cycle (Pacheco *et al.* 1993).

The 1995 October 9 ($M_w = 8.0$) Colima–Jalisco earthquake (Figs 1 and 2) was one of the few earthquakes in the past century to have occurred close enough to a GPS geodetic network to study the coseismic and near-term post-seismic behaviour of the subduction fault interface. This earthquake was the first significant rupture of the Middle America Trench northwest of the Manzanillo Trough since the 1932 June 3 ($M_w = 8.2$) and 1932 June 18 ($M_w = 7.8$) earthquakes (Singh *et al.* 1985). Earthquake focal mechanisms for the 1995 October 6 ($M_w = 5.8$) foreshock, the main shock, and the 1995 October 12 ($M_w = 6.0$) aftershock (Dziewonski *et al.* 1997, Escobedo *et al.* 1998) are consistent with shallow thrusting in a direction 5–10° anticlockwise from both the N40°E Rivera–North America convergence direction (DeMets & Wilson 1997) and the direction normal to trench. Inversions of surface and body waves recorded at local and teleseismic distances (Courboulex *et al.* 1997; Escobedo *et al.* 1998; Mendoza & Hartzell, 1999) indicate that the rupture initiated at a depth of 15–20 km near the northwest edge of the Manzanillo Trough and propagated ~150 km to the northwest. The rupture consisted of several subevents, the largest of which began 35–40 s after the initial rupture and affected shallow regions of the subduction fault ~100 km northwest of the Manzanillo Trough (Courboulex *et al.* 1997, Escobedo *et al.* 1998). The coseismic displacements of 11 GPS sites (Melbourne *et al.* 1997) are best fit by a model in which the majority of the seismic moment was released in two patches, one near the northwest edge of the Manzanillo trough and the other ~80–120 km farther northwest. The geodetic and seismologic results thus concur with the conclusion that this was a multiple-source earthquake.

We use GPS geodetic measurements at 26 sites in the Colima–Jalisco region to characterize the kinematics and dynamics of this large subduction zone earthquake. The Jalisco–Colima GPS network encompasses the coseismic rupture zone in both directions along the trench (Fig. 1) and includes the area of the elastic strain field with high horizontal and vertical displacement gradients. Both factors are critical for resolving details of the fault geometry and the distribution of fault slip. The observations consist of GPS-derived horizontal and vertical displacements that extend from seven months before the Colima–Jalisco earthquake to ~3.5 years after.

2   NEOTECTONIC SETTING

The tectonic setting of the Jalisco–Colima GPS network (Figs 1 and 2) is dominated by northeast-directed subduction of the Rivera and Cocos Plates beneath the western edge of the North American Plate. Northwest of the Rivera–Cocos–North America trench–trench–fault triple junction, the Rivera Plate subducts beneath North America at rates that decrease from 38 ± 4 mm yr^{-1} (2σ) at the Manzanillo trough to only 15 ± 3 mm yr^{-1} at 20.8°N (DeMets & Wilson 1997). Southeast of the triple junction, the Cocos Plate subducts at 51 ± 2 mm yr^{-1} (Fig. 2), implying that motion occurs between the subducting Rivera and Cocos slabs beneath the continental margin.

The subduction of young (<11 Myr) oceanic lithosphere along the northern end of the Middle America Trench appears to have profoundly influenced the neotectonics of the overlying North American Plate, particularly in the vicinity of the Jalisco Block (JB in Fig. 1). The Jalisco Block is an elevated region bounded on the north and the east by linear depressions characterized by active faulting and abundant young volcanism. One of the structures that bounds the Jalisco Block, the Colima Graben (CG in Fig. 1) has been active for ~5 Myr and appears to lie above the subducting Rivera–Cocos Plate boundary (Bandy *et al.* 1995). The other bounding structure, the Tepic–Zacoalco fault zone, extends NW from the northern end of the Colima Graben to the Gulf of California and consists of a series of en echelon fault-bounded basins attributed to oblique dextral opening (Allan 1986) followed by orthogonal extension (Rosas-Elguera *et al.* 1996; Ferrari & Rosas-Elguera 2000). Fault slip rates inferred from geological data are poorly known, but are probably slower than several millimetres per year (Allan 1986; Allan *et al.* 1991; Serpa *et al.* 1992; Ferrari *et al.* 1994; Righter *et al.* 1995).

## 3   GPS DATA: ANALYSIS, DISPLACEMENTS AND UNCERTAINTIES

3.1   Network description

The Jalisco–Colima GPS network consists of 26 geodetic benchmarks located in the Mexican states of Jalisco, Colima and Michoacan (Table 1 and Fig. 3). The network extends from the Pacific coast 350 km inboard to the North American Plate interior, spanning the Jalisco Block and its bounding faults. Thirteen of the benchmarks were installed prior to the Colima–Jalisco earthquake and the remainder in early 1996 or later. One site (TOMA) was abandoned after two occupations and a second (LIMA) was replaced with a more accessible nearby monument (LIM2). All of the benchmarks consist of 15–25 cm long steel or brass pins or markers. 20 of the benchmarks are epoxied into bedrock or large boulders and the remainder into solid cement structures, including two buildings (UGEO and UMON). Sky visibility is good to excellent at all sites.

Except for data from sites COOB, UGEO, and CRIP, which operated semi-continuously after early 1997, our GPS observations come from annual network occupations between March 1995 and March 1999 (Table 1). Annual occupations coincided with the winter dry season in an effort to minimize seasonal and tropospheric noise. We used Trimble 4000 SSE dual-frequency, code-phase receivers and Trimble SST antennae with ground planes throughout the experiment to avoid displacement artifacts that can be introduced via differing receiver/antenna combinations. Measurements in March 1995 and October 1995 consisted mostly of one, two or three 8 hr sessions, while measurements during and after 1996 typically lasted 30–60 hrs (Table 1).

3.2   GPS data analysis procedures

All GPS data were analysed using GIPSY-OASIS software (release 5) (Zumberge *et al.* 1997), free-network satellite orbits and satellite clock offsets obtained from the NASA Jet Propulsion Laboratory and the precise point positioning analysis strategy described by Zumberge *et al.* (1997). Site coordinates determined
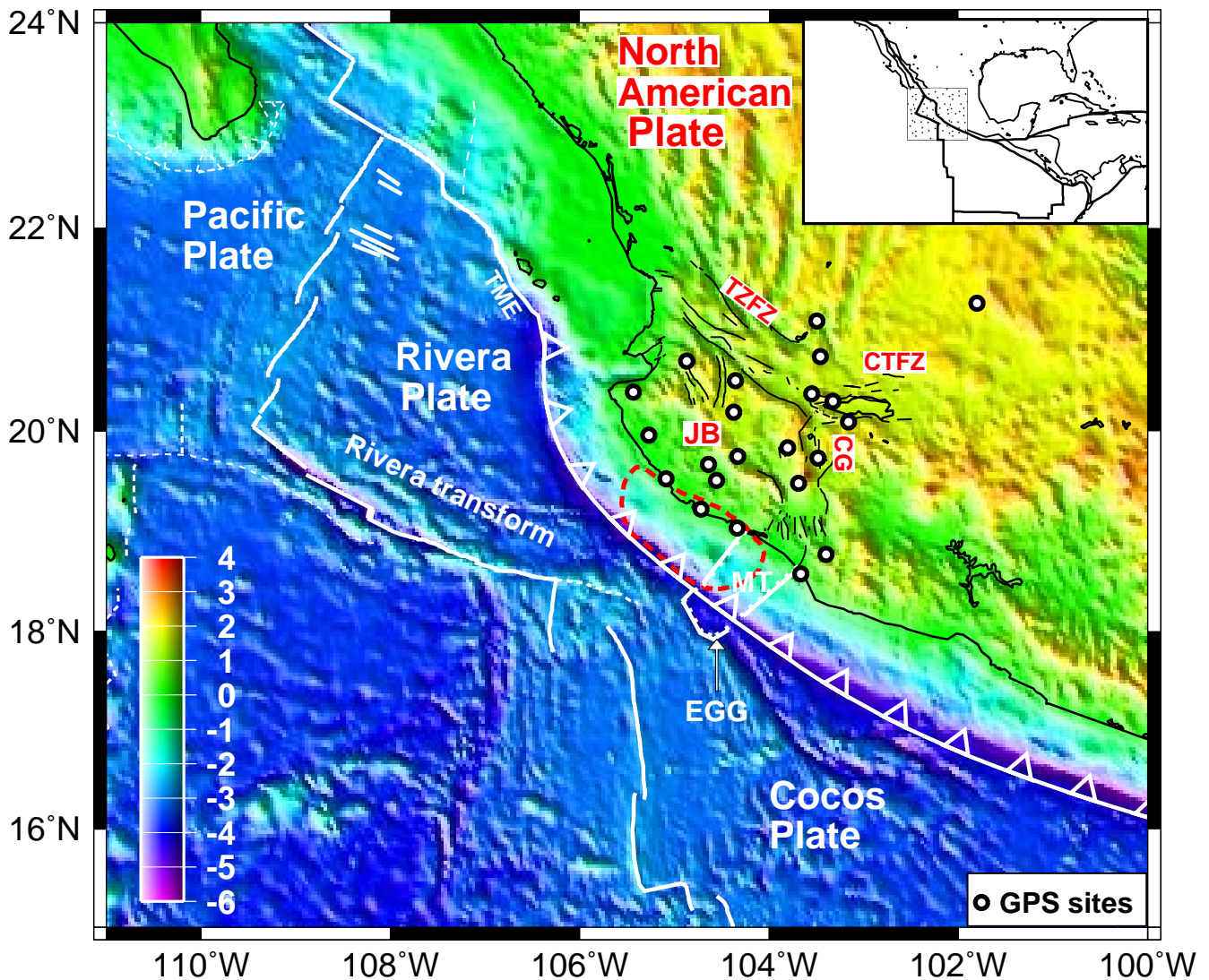
Figure 1. Principal features described in text and GPS site locations. Solid and dashed lines designate active and inactive tectonic features, respectively. Red dashed line designates the rupture zone of the 1995 October 9 Colima–Jalisco earthquake. Abbreviations are CG, Colima Graben, CTFZ, Chapala-Tula fault zone, EGG, El Gordo graben, JB, Jalisco Block, MT, Manzanillo trough, TZFZ, Tepic-Zacoalco fault zone TME, Tres Marias escarpment. Topography and bathymetry are illuminated from the southwest and are from Smith & Sandwell (1997) and Sandwell & Smith (1997).

from our analysis of the GPS phase and pseudo-range observables are initially defined in a fiducial-free reference frame and subsequently transformed into the International Terrestrial Reference Frame 1997 (ITRF97) (Boucher *et al.* 1999) using seven parameter Helmert transformations that align the daily coordinates of a selected subset of ITRF97 fiducial sites with the fiducial-free coordinates of the same subset of sites. The coordinates for individual GPS sessions are used to assess day-to-day location repeatability, identify outliers, determine the mean coordinates for multiple-session site occupations, and ultimately, derive the interval displacements relative to the North American Plate needed for modelling the evolution of slip along the subduction interface.

The most important differences in our analysis procedures compared to those applied by Melbourne *et al.* (1997) to the GPS data collected in March and October of 1995 arise from the reference frames that are used to describe the coseismic displacements. All displacements given in Melbourne *et al.*

(1997) are specified relative to ITRF94, the most widely used geodetic reference frame available at the time. We instead employ ITRF97, a significantly improved version of ITRF (Sillard *et al.* 1998; Boucher *et al.* 1999) and transform the displacements to a North American Plate reference frame (see Section 3.4).

3.3 Uncertainties in site coordinates

Accurate estimates of uncertainties in 3-D site coordinates are essential for discriminating between alternative fault-slip models and hence are an important part of the analysis. Noise in the GPS-measured displacements includes at least two important components; white noise over periods of days or less and longer-period noise due to random walk of the GPS benchmark and other more poorly understood factors such as seasonal variations in temperature, atmospheric pressure and ocean tidal loading (Langbein & Johnson 1997; Zhang *et al.* 1997; Mao *et al.* 1999).

Table 1. GPS sites and occupation history.

Site ID	Monument Type	Lat. (°N)	Long. (°W)	Cumulative hours of data						
				3-95	10-95	12-95	3-96	2-97	3-98	3-99
AUTA	cement pad	19.748	104.330	–	–	–	31	24	42	38
AVAL	boulder	19.481	103.685	24	26	20	34	17	42	61
AYUT	bedrock	20.188	104.375	24	8	–	33	32	42	67
CEBO	bedrock	20.090	103.160	24	8	–	32	–	42	45
CGUZ	bedrock	19.730	103.446	–	–	–	32	–	42	62
CHAC	bedrock	20.384	105.429	24	21	–	35	37	42	63
CHAM	bedrock	19.527	105.084	24	24	–	36	38	42	66
COOB	cement pad	19.381	103.674	–	–	–	–	SC[1]	SC	SC
COSA	boulder	20.293	103.325	–	–	–	32	17	38	44
CRIP	bedrock	19.032	104.333	120	224	62	182	117	40	SC
GUAC	bedrock	20.501	104.354	24	8	–	33	36	42	62
GUFI	cement pad	19.506	104.550	–	–	–	32	36	42	64
JARA	bedrock	21.263	101.800	–	–	–	32	38	42	63
LIMA	bedrock	20.370	103.548	–	–	–	29	12	42	–
LIM2	boulder	20.335	103.528	–	–	–	–	–	46	46
MCAB	bedrock	21.092	103.494	24	–	–	32	38	42	62
MELA	bedrock	19.220	104.718	–	–	–	30	36	42	64
PURI	bedrock	19.665	104.637	24	17	–	28	24	42	64
SAUZ	bedrock	20.885	103.225	–	–	–	–	39	–	40
SEBA	bedrock	20.699	104.871	24	–	–	36	–	42	62
SJDL	bedrock	18.576	103.663	24	25	16	32	38	42	72
TAPA	bedrock	19.831	103.797	24	7	–	19	–	42	62
TOMA	cement pad	19.960	105.269	–	–	–	20	19	–	–
UGEO	building	20.694	103.350	–	–	–	–	–	SC	SC
UMON	building	20.737	103.453	–	–	–	48	302	48	43
VICT	bedrock	18.768	103.396	24	26	–	38	19	42	62

1—SC designates semi-continuously operating site.

We derived a realistic estimate for the magnitude of daily white noise by comparing site location uncertainties derived within GIPSY (hereafter referred to as the formal uncertainties) to uncertainties derived from the day-to-day differences in the coordinates and heights of a given site. The formal uncertainties in the 3-D site location are propagated directly from estimates of noise in the GPS phase and pseudo-range observables and the *a priori* model parameters, but exclude other potential sources of errors such as unresolved carrier phase ambiguities, unmodelled GPS signal multi-path, unmodelled oceanic tidal loading for coastal sites and errors in tripod set-up and/or antenna height measurements. Daily scatter for a given site is specified relative to its mean 3D location over the few-day period it was occupied during a given year.

Formal uncertainties in the daily locations of sites occupied during the March 1995 field campaign, during which the GPS sessions averaged only 8 hrs, average ± 3 mm in latitude (north), ± 7 mm in longitude (east) and ± 16 mm in height. In contrast, the day-to-day scatter in the site locations for the March 1995 data is ± 7 mm (1σ), ± 15 mm, and ± 24 mm for the north, east, and vertical components. The uncertainties estimated from the daily scatter thus exceed the formal uncertainties by factors of 1.5–2.3 for this campaign. A similar comparison was not possible for the October 1995 field campaign because nearly all sites were occupied for only a single session. Data collected during the longer 12–24 hr sessions characteristic of occupations during and after March 1996 yield a similar result, with formal uncertainties in the north (± 2 mm), east (± 3 mm), and vertical ($\pm 7$ mm) components that are 2.6–2.7 times smaller than the day-to-day scatter in the north (± 5 mm), east (± 9 mm), and vertical (± 19 mm) components (Fig. 4).

The uncertainties estimated from the daily scatter thus exceed those propagated from the GPS data noise by factors of 1.5–2.7, in good accord with results reported by other authors (e.g. Savage *et al.* 1994; Hudnut *et al.* 1996; Donnellan & Lyzenga 1998). We thus increased the formal uncertainties in all three components of the site locations by a factor of 2.5 and propagated these uncertainties into all aspects of the analysis described below. Correlations between the north, east and vertical are small and are ignored hereafter.

Given the infrequency of our network occupations, it is more difficult to quantify the magnitude of noise over periods longer than several days. We note however that the displacement paths for nearby GPS sites (Figs 5–8) agree remarkably well, even after 1997 when most sites in the network move only 5–20 mm annually. Such good agreement would not be expected if the cumulative uncertainties in the north or east components significantly exceeded $\sim \pm 10$ mm. Given that ± 10 mm is the approximate magnitude of the day-to-day scatter in the site locations, long-period noise appears to contribute little to the error budget and is ignored hereafter.

### 3.4 North American Plate reference frame

For our purposes, the motions of sites in the Jalisco–Colima GPS network are best described relative to a North American Plate reference frame. We derived the angular velocity that best describes the motion of the North American Plate relative to
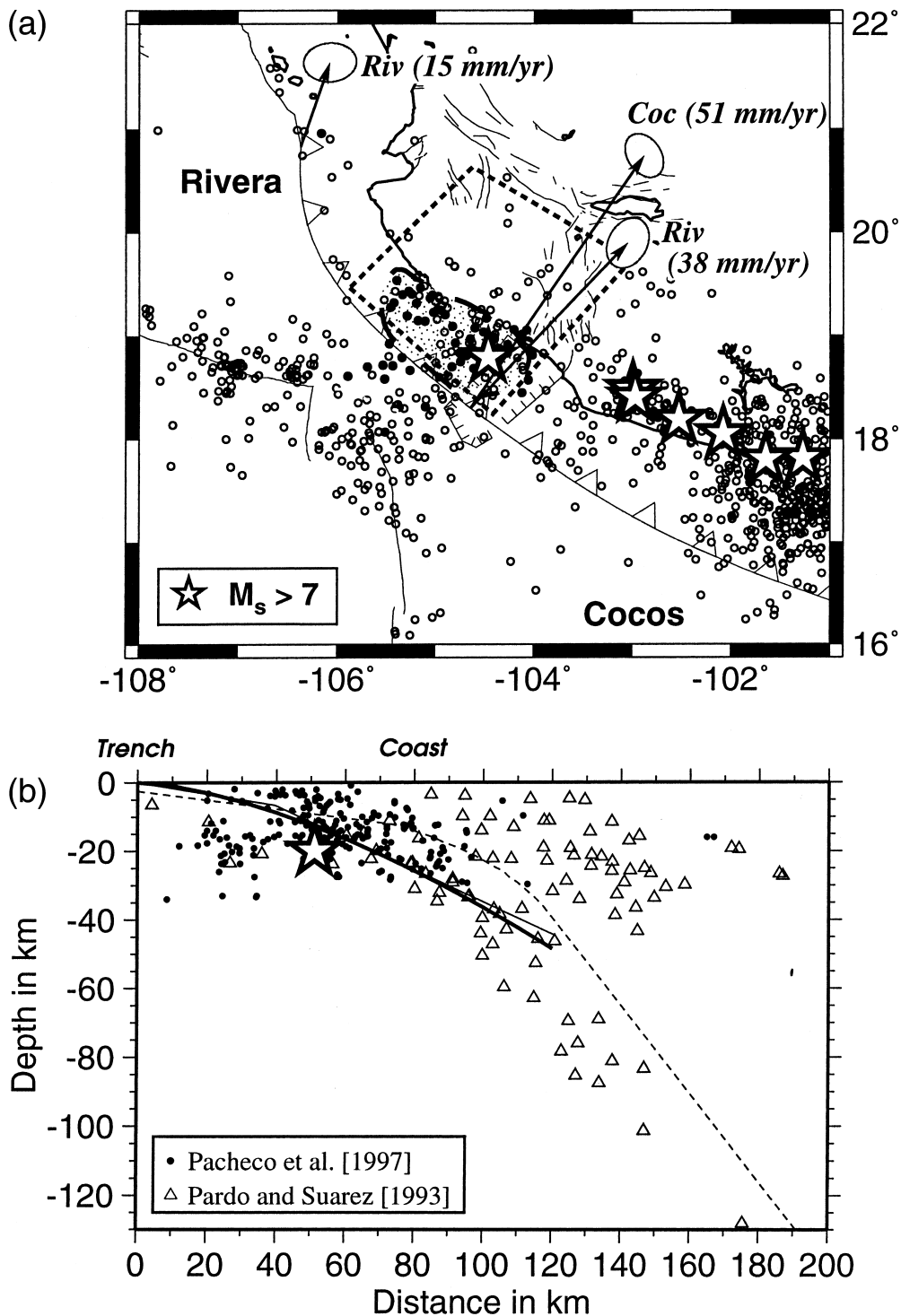
Figure 2. (a) Shallow-focus earthquakes along the northern Middle America Trench for the period January 1967–January 2000 from the USGS earthquake catalog. Vectors and ellipses show 0.78 Ma-average velocities and 2-D 95 percent uncertainties for Cocos-North America and Rivera-North America motion (DeMets & Wilson 1997). Shaded region shows rupture area of 1995 October 9 earthquake and filled circles show earthquake aftershocks. (b) Trench-normal vertical profile (N45°E) of earthquakes from Pardo & Suárez (1993) and Pacheco *et al.* (1997). Bold and thin lines show the best curved-fault and two-fault geometries derived from the geodetic data (see Section 5.1). Dashed line shows the Benioff zone geometry proposed by Pardo & Suárez (1993) and Pardo & Suárez (1995).

ITRF97 by inverting the horizontal velocities of 16 continuously operating GPS stations in the North American Plate interior. Details regarding the procedures used to invert these velocities are given by DeMets & Dixon (1999). The stations we use,

shown in Fig. 1 of DeMets and Dixon (1999), have operated continuously for periods ranging from 3.8–7.0 yr and have well-constrained velocities. We analysed all of the GPS data underlying these station velocities using the same strategies and
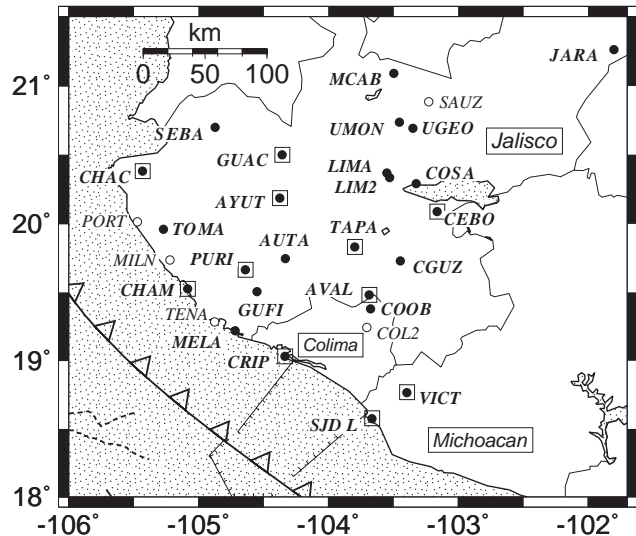
Figure 3. Locations of GPS sites in the study area. Solid circles denote sites with data used in this study. Squared circles represent sites occupied before and after the 1995 October 9 earthquake. Open circles denote sites installed in 2000 and less-frequently occupied sites. Names of Mexican states are in boxes.

software as described in Section 3.2 so as to minimize the possibility that a subtle difference in reference frame definition or data analysis procedures might introduce a systematic bias into the GPS displacements used for our modelling.

The North America-ITRF97 rotation that best fits the 16 North American GPS station velocities predicts an annual displacement of 12.7 ± 0.3 mm (1σ) toward S38.6°W±2.6° for a point in the middle of the Jalisco GPS network. Velocities predicted by the best-fitting rotation vary minimally across the small-aperture Jalisco network. GPS site displacements and displacement uncertainties relative to North America were derived via vector subtraction and linear propagation of errors. The uncertainties in the predicted plate displacements are a factor of $\sim$10–20 smaller than the uncertainties in our measured GPS site displacements and thus constitute only a small part of the overall error budget. The effect of possible slow motion of the Jalisco Block relative to North America on our modelling results is discussed in Section 6.6.
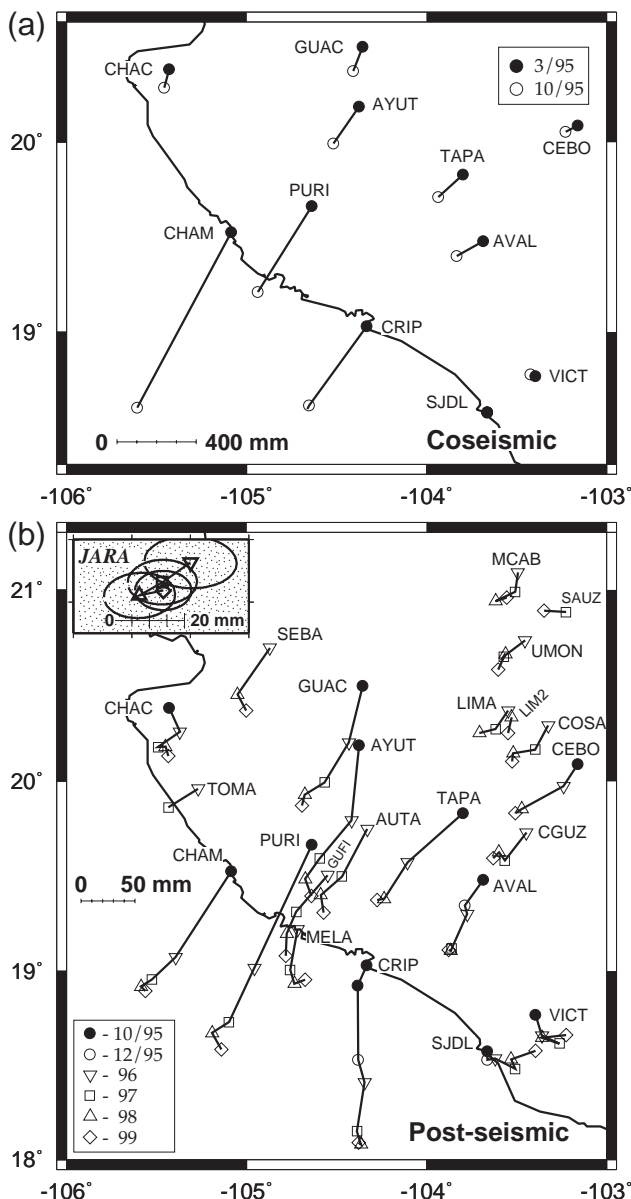
3.5 Horizontal displacements

The observed site displacements show excellent coherence in space (Fig. 5) and through time (Fig. 6). For example, the coseismic horizontal displacements decrease with distance from the seismically-defined offshore rupture zone and are directed uniformly inward toward the rupture. They are thus consistent with an elastic response to the coseismic rupture, as shown by Melbourne *et al.* (1997). Most sites in the network continued to move toward the rupture zone after the 1995 October 9 earthquake (Fig. 5), but at rates that decreased through time (Fig. 6). Detailed comparison of the post-seismic displacements for nearby sites shows that the slip directions of many sites changed in concert at least once since the earthquake, possibly signaling one or more redistributions of slip along the sub-duction interface. After March 1998, the trenchward motions
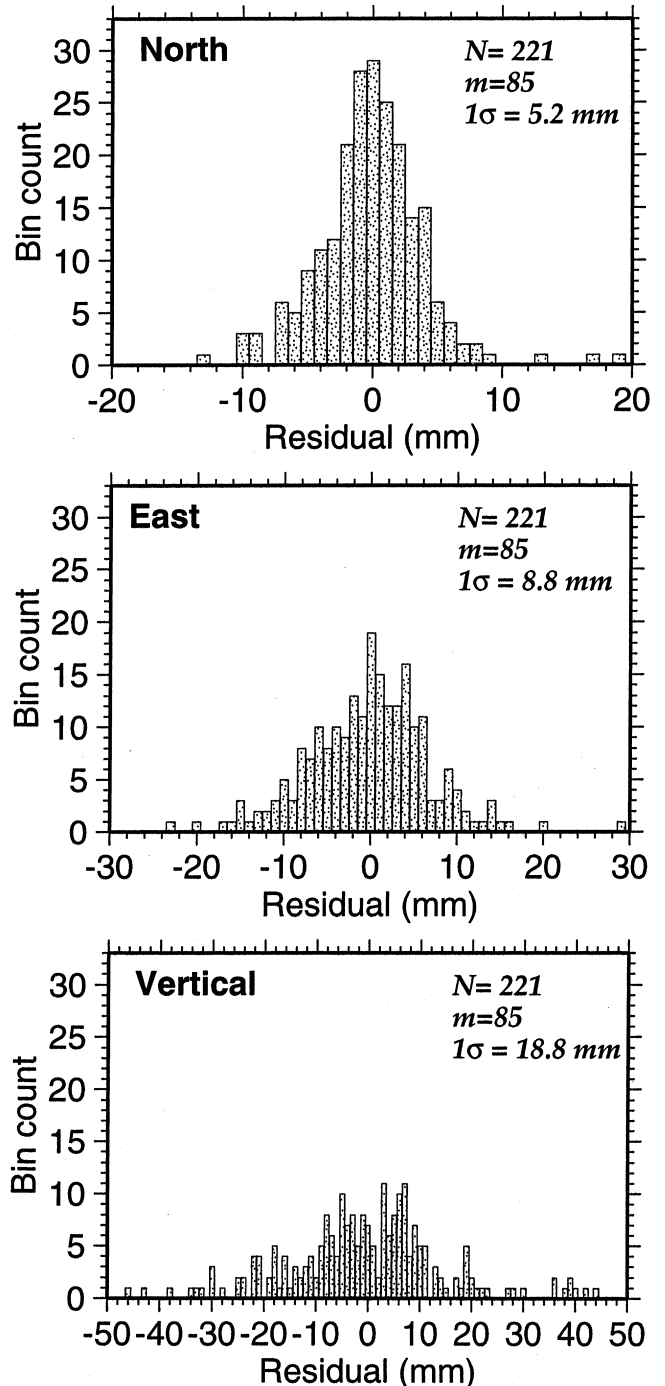
Figure 4. Residual distances in millimetres in the north, east, and down components of daily site locations relative to multi-day mean site locations for the period 1996–1999. N is the number of station-days for which individual site positions are used; m is the number of multi-day means determined from those station-days and 1σ designates the value that brackets 68.3 percent of the residual distances.

of several coastal sites (CRIP, MELA, and CHAM) largely ceased, suggesting relocking of the shallow portions of the subduction interface. Detailed modelling and interpretation of these displacements is presented in Section 6.

Unlike other sites in the network, which translated SSW in the years following the earthquake, sites SJDL and VICT translated ESE relative to stable North America. We can think

Figure 5. (a) Observed horizontal displacements relative to North American Plate during March 1995–October 1995, spanning the Colima–Jalisco earthquake. Ellipses show 2-D, 1σ uncertainty regions. (b) Observed horizontal displacements relative to North American Plate following the 1995 October 9 earthquake. Uncertainty ellipses are omitted for clarity, but are shown in inset for site JARA to emphasize that its motion relative to the North American Plate interior is slow or zero. Two consecutive 5-day-average locations shown for CRIP for the October 1995 field campaign illustrate rapid post-seismic motion after the earthquake.

VICT only for the coseismic interval (March 1995–October 1995), during which their motions were dominated by the 1995 October 9 earthquake.
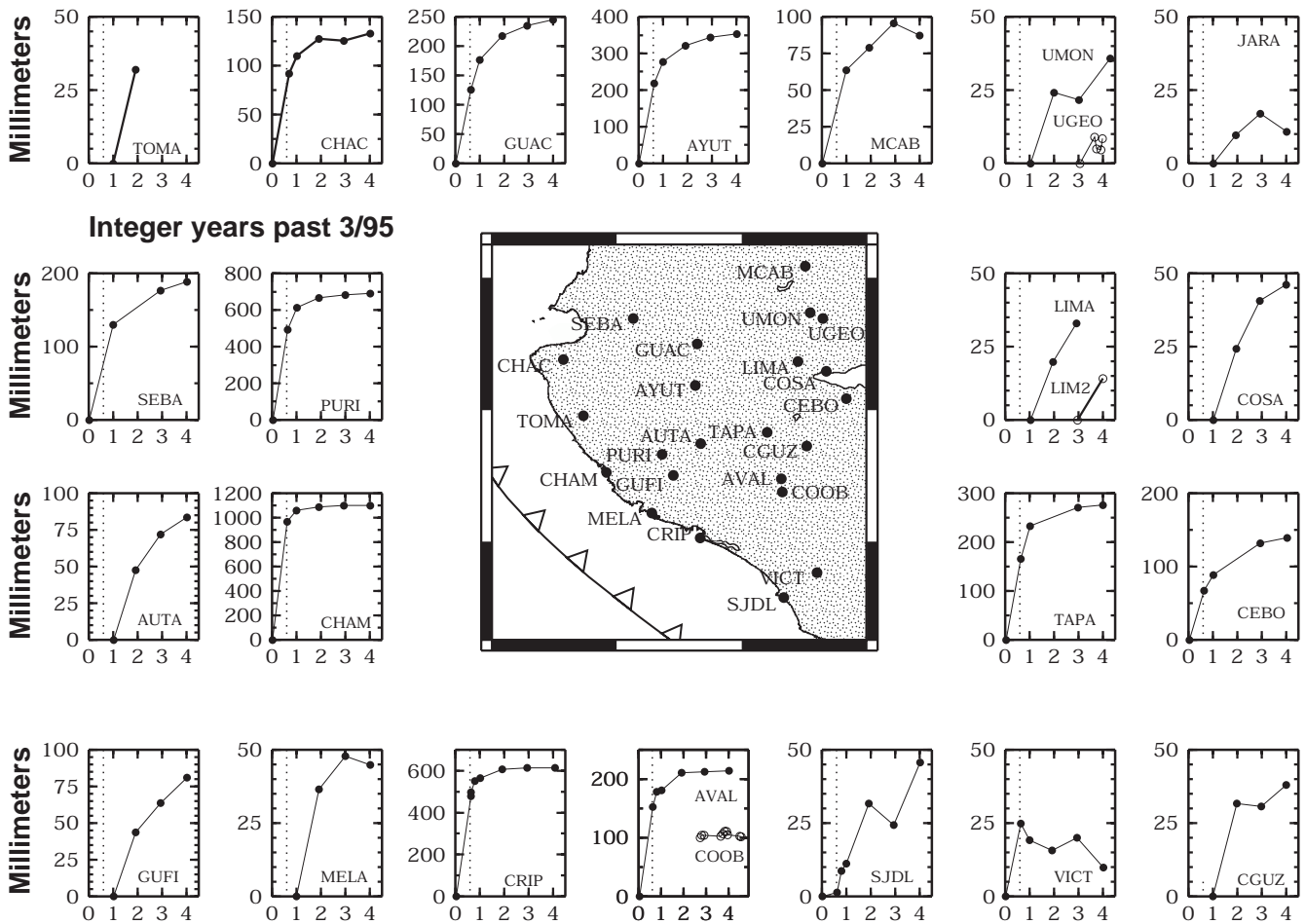
3.6 Vertical displacements

The vertical displacements also display excellent coherence in space and time (Figs 7 and 8) despite their higher uncertainties. All sites subsided during the 7 month interval spanning the Colima–Jalisco earthquake (bottom panel of Fig. 7), with the subsidence decreasing away from the rupture zone. During the 5 month period immediately following the earthquake (October 1995–March 1996), the vertical motions of all but one site reversed relative to their coseismic displacements, yielding regional uplift (Fig. 7) that decreased in magnitude with distance from the rupture zone. Between March 1996 and February 1997, the three sites nearest the rupture zone (MELA, CRIP, and CHAM) experienced uplift whereas the other sites subsided, including the remaining coastal sites CHAC, SJDL, TOMA, and VICT. Subsidence at SJDL and VICT may be a response to the 1997 January 11 ($M_w = 7.2$) earthquake ~ 100 km southeast of these sites. Subsidence at TOMA and CHAC may be evidence for aseismic slip of unknown duration along the northernmost Rivera subduction zone (see Section 6.3). Vertical displacements between February 1997 and March 1998 mimic the pattern of the previous period, with uplift observed at the coastal and near-coastal sites and subsidence at many sites farther inboard. Vertical displacements during this and the following interval (March 1998–March 1999) average 10–20 mm and are thus closer to their uncertainties (Fig. 4). In general, the most robust aspect of vertical displacements after February 1997 is continued uplift of the coastal sites. Extending the time series at other sites in the network will help to determine whether the pattern of regional uplift manifested between March 1998 and March 1999 is real or merely an expression of spatially-correlated noise in the GPS site coordinates.

4 MODELLING TECHNIQUES

4.1 Singular value decomposition

We derived the optimal distribution of slip along the subduction interface for a given time interval using singular value decomposition (SVD) (Harris & Segall 1987; Segall & Matthews 1988; Lundgren *et al.* 1999). We refer the reader to Harris & Segall (1987) for a thorough exposition of the technique and summarize only those aspects of the technique relevant to this analysis.

Given a set of N measured geodetic displacements and a fault composed of k rectangular elements, with $k > N$, singular value decomposition of the matrix that specifies the elastic response at each geodetic site to unit slip along each subfault produces k singular values and model terms that fully specify the distribution of fault slip. Many of the small singular values are statistically insignificant and can be eliminated without significantly degrading χ^2, the weighted least-squares misfit. The variation in χ^2 as a function of the number of singular values can thus be used to identify the simplest distribution of slip that fits the observations at a statistically acceptable threshold or a threshold acceptable to the user. By its nature, SVD facilitates minimization of reduced chi-square $\chi^2_v = \chi^2/(N - v)$, where v represents the number of parameters used to fit the data.

of at least two reasons for their discordant motions. Both sites are separated from the remainder of the network by the Colima Graben, a prominent upper crustal discontinuity that may wholly or partly decouple the motions of SJDL and VICT from those of the remaining sites. In addition, both sites lie above the Cocos–North America subduction interface and thus probably have motions that are more strongly influenced by strain accumulation caused by NE-directed Cocos–North America convergence than are the motions of the other sites in the network. For these reasons, we model the displacements at SJDL and

Figure 6. Horizontal displacements in mm (vertical axis) versus time in years from March, 1995 (T = 0). Dotted line shows time of 1995 October 9 earthquake. Displacements for site LIM2, located ∼2 km from LIMA, are shown in panel for LIMA. Uncertainties are eliminated for clarity, but are typically ±5–10 mm.

We implement SVD using a modified version of the GINV software described in Larsen (1991). The key modifications include calculation of elastic displacements using equations from Okada (1985) instead of Mansinha & Smylie (1971) and calculation of data importances. We assume hereafter that the observed surface displacements can be modelled as a response to dislocations along rectangular fault elements embedded in a uniform elastic half-space. Misfits to the geodetic displacements arise from errors in the observed displacements, errors in the fault parameterization, deviations of the lithosphere from an idealized elastic response and, to a lesser extent, departures of Poisson's ratio from its assumed value of 0.25.

SVD is conducive to rigorous determinations of model and data resolutions. The diagonal elements of the model resolution matrix specify how well slip is resolved for individual sub-faults and range from zero for unresolved slip to one for perfectly-resolved slip. Because the resolution of slip for a given sub-fault can be reduced arbitrarily by decreasing the size and hence increasing the number of subfaults, the absolute magnitude of the resolution for an individual subfault is a less useful measure of where slip is well resolved than are the relative variations in model resolution across the entire fault or the integrated

resolution of slip within major slip patches. All slip distributions displayed in Section 6 are accompanied by plots of fault-slip resolution, emphasizing where fault slip is best constrained.

The diagonal elements of the data resolution matrix (Menke 1984) are termed data importances and yield a formal measure of the amount of information provided to the model by an individual datum. The importance of an individual datum depends entirely on its estimated uncertainty and the sensitivity of the model's predictions at a given geographic location to changes in the model parameters. The cumulative data importance equals the total number of adjustable parameters (i.e. singular values). The information contributed by displacements from the sites along and near the coast dominate our estimates of slip along the subduction interface because small changes in the distribution of fault slip induce large changes in the predicted displacements for those sites. Sites distant from the subduction zone contribute negligible information to the solution because large changes in the slip distribution produce only small changes in their predicted surface displacements.

We minimize short-wavelength, poorly-resolved variations in fault-slip by two techniques; truncation of all singular values that fail to significantly improve the least-squares fit and use of
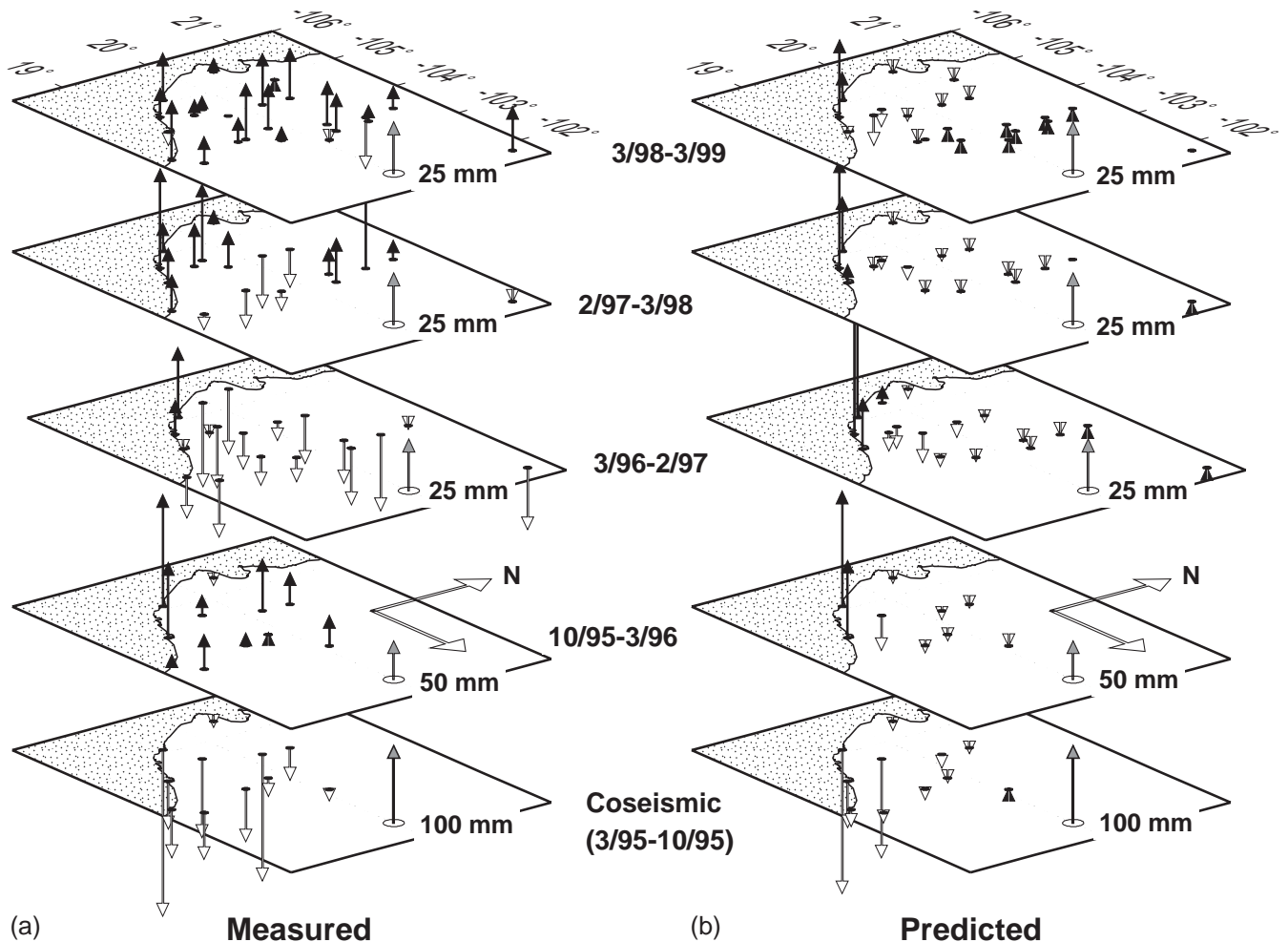
Figure 7. Oblique views of the measured (a) and predicted (b) vertical displacements (Table 2). Solid and open arrows represent uplift and subsidence, respectively. Scale is given by arrows that are circled at their origins.

the coarsest discretization of the subduction interface that does not significantly degrade the model fit. Details regarding each are given in Sections 5.2 and 5.3. No other smoothing is employed.

### 4.2 Testing for significant changes in the pattern of fault slip

An important goal of our analysis is to test for significant changes in the pattern of slip along the subduction interface through time. To do so, we designed a test that compares the least-squares fits of two fault-slip models. The first, a stationary-slip model, requires the pattern of fault slip to remain identical for two or more successive time periods, but allows for a scale difference in the slip magnitudes. It is derived by simultaneously inverting GPS displacements for two (or more) successive intervals to solve for the k singular values and linear scaling constant that yield the lowest least-squares misfit to the combined sets of observations. The second model for fault-slip imposes no constraints on the patterns of fault slip for successive periods and is derived by separately inverting GPS displacements for two (or more) successive intervals to solve for the k singular values for each interval that best fit the observations for that interval in a least-squares sense. For a two-interval test,

the number of parameters adjusted to fit the data is thus $2*k$. Fewer parameters ($2*k-k-1$) are thus used to construct the simpler, stationary-slip model. The F-ratio test for additional model terms (Bevington & Robinson, 1992) is used to evaluate whether the least-squares fit of the stationary-slip model is significantly worse than that of the best-fitting models.

5 OPTIMIZATION OF THE MODEL PARAMETERS

5.1 Geometry of the subduction interface

Earthquake hypocenters along a profile perpendicular to the Rivera subduction zone (Fig. 2) clearly show that the dip of the subducting plate changes with depth (Pardo & Suárez, 1993), but are too imprecisely located to define the fault geometry at the level of precision required for geodetic modelling. We therefore establish the best geometry for the subduction interface by examining how the fits to the coseismic displacements, which have the highest signal-to-noise ratio of the five intervals we measured, vary as a function of fault geometry. We explore three classes of fault geometries, namely, curved geometries in which the dip of the subduction interface increases with
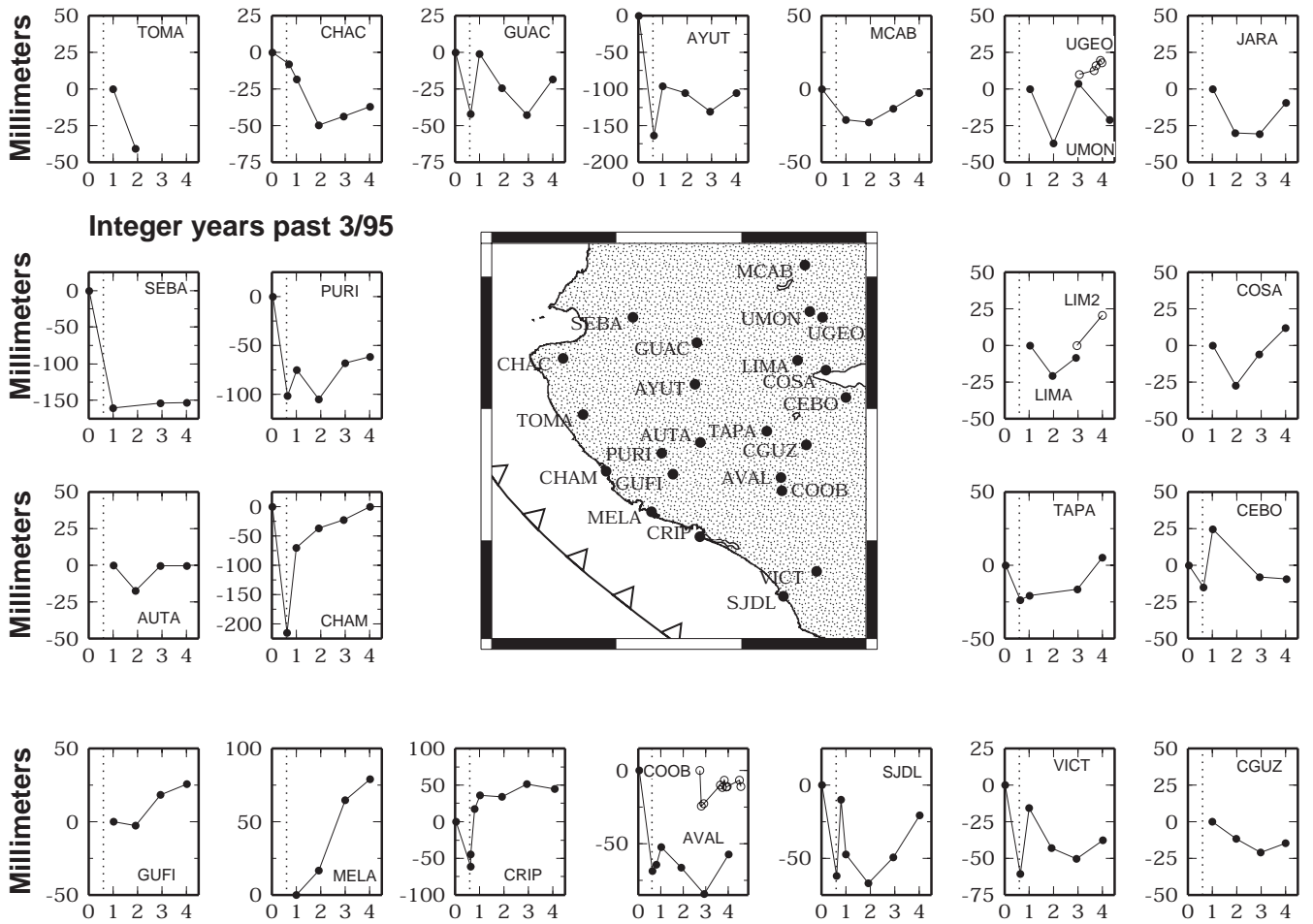
Figure 8. Vertical displacements in mm (vertical axis) versus time in years from March, 1995 (T = 0). Vertical position is measured relative to the height determined from first-epoch measurements. Dotted line shows time of 1995 October 9 earthquake. Displacements for site LIM2, located ~2 km from LIMA, are shown in panel for LIMA. Uncertainties are eliminated for clarity, but are typically ±10 mm.

distance from the trench, single planar fault geometries, and two-segment geometries with an upper, shallow-dipping fault and a lower, more steeply-dipping fault. We employ an azimuth of N50°W for the subduction fault, in accord with the trench morphology. We use an along-strike fault length of 220 km, which significantly exceeds all seismologic estimates for the length of the rupture zone, and divide the subduction interface into non-overlapping, rectangular sub-faults that extend 20 km along-strike and 10 km downdip (see Section 5.2) to a depth sufficient to capture all slip.

Given the relatively small ~5–10° difference between the observed trench-normal direction and the N29°E–N36°E horizontal slip directions derived from focal mechanisms for the Colima–Jalisco earthquake and its largest foreshock and aftershock (Dziewonski *et al.* 1997; Escobedo *et al.* 1998), we constrain slip in our model to be purely dip-slip. Inversions of the coseismic displacements that allow for both dip-slip and strike-slip components along the fault yield a pattern of dip-slip motion close to that for a pure dip-slip solution, indicating that our assumption of pure dip-slip motion is adequate.

Continuous curvature faults can be described using an equation of the form $d = Ax^n$, where d is the vertical depth to the subduction interface, x is the distance in km from the trench along a great circle orthogonal to the trench, and A and n

are unknowns that specify the curvature of the fault. Fault geometries in this class are less complex than the two-segment faults described below because only two parameters are needed to describe the fault geometry. We inverted the coseismic displacements while progressively changing the values for A and n to represent fault geometries that range from planar faults that dip only 1° to steeply dipping, curved faults. The 2-D χ^2 solution space for A and n is well behaved and exhibits a single, well-defined minimum at $n = 1.55$ and $A = 0.0290$ with a least-squares misfit of 166.2. The implied fault geometry (Fig. 2) agrees well with the independent seismic constraints. None of the planar fault geometries (i.e. those for which $n = 1$) fit the data within the statistical limits prescribed by the best-fitting solution.

We investigated the fit of two-fault geometries by varying the upper and lower fault dips and the downdip extent of the upper fault through a range of values consistent with the seismic constraints. The geometry that fits the data best (thin line in Fig. 2) has an upper fault segment that extends 40 km downdip at a dip of 9.5°, where it intersects a lower segment that dips 25°. This geometry agrees well with the best curved-fault geometry (Fig. 2) and has a least-squares fit of $\chi^2 = 138.0$, superior to that for the best curved fault geometry. A comparison of the two fits using an F-ratio test for the appropriate degrees of

freedom however indicates that the improvement in fit is not significant at the 99 per cent confidence level. In addition, displacements for three of the four post-seismic periods are fit better if we use the best curved fault geometry than a two-segment geometry, with overall differences in the fits of both geometries of only 1–5 per cent. We thus use the best curved fault geometry for the remainder of the analysis. None of the results presented below would change significantly if we instead used the best two-segment geometry.

5.2 Sub-fault dimensions

We next tested the sensitivity of our fault-slip solutions to the assumed dimensions of the sub-faults that are used to discretize the curved subduction interface. Using seven singular values to describe the slip distribution, we repeatedly inverted the coseismic displacements while decreasing the downdip dimension of the subfaults from 40 to 5 km in 5-km increments. The least-squares fits improve as the downdip dimension is decreased from 40 to 10 km, but improve only marginally for dimensions smaller than 10 km. Similarly, inverting coseismic displacements while decreasing the along-strike sub-fault dimension from 100 to 10 km yields fits that improve consistently until the along-strike dimension reaches 20 km, below which no further improvement in fit occurs. We conclude that subfaults with respective along-strike and downdip dimensions of 20 and 10 km discretize the subduction interface sufficiently well to characterize the underlying slip distribution. Given that the overall along-strike and downdip fault dimensions are 220×120 km, the subduction interface is divided into 132 rectangular fault elements. Extension of the fault farther than 120 km downdip does not significantly improve the fit to displacements for the coseismic or later intervals, indicating that slip beneath depths of ~ 40 km is not required by the data.

5.3 Truncation of singular values for a minimum-complexity model

Fig. 9 displays the dependence of the least-squares misfit χ^2 for each of the five intervals we modelled (Table 2) on the number of singular values k and hence the number of model terms used to describe their corresponding best-fitting distributions of fault slip. The fit for the coseismic interval (March 1995–October 1995) and first post-seismic interval (October 1995–March 1996) improves rapidly for singular values $k=1–7$, but improves only marginally if we employ singular values beyond $k=7$ to describe the slip distributions. The fit to displacements for the period March 1996–February 1997 improves rapidly until $k>4$, after which slow but significant improvements in the fit continue until $k=9$. Displacements for February 1997–March 1998 are well-fit using only four singular values, whereas the fits to displacements for March 1998–March 1999 improve gradually until $k=7$.

Table 3 summarizes further characteristics of the candidate fault-slip solutions for each of the five intervals we modelled. In general, model terms with signal-to-noise ratios that exceed $\sim 4–5$ are associated with significant improvements in the corresponding least-squares fit (Fig. 9). The model variances for each interval represent the roughness of the slip distribution associated with a given number of model terms (Harris & Segall
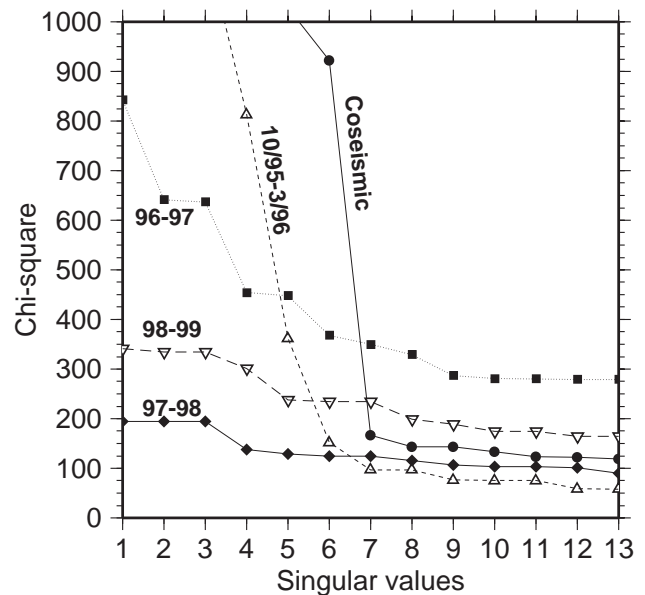
Figure 9. Least-squares fits to displacements for the coseismic and post-seismic intervals as a function of the number of singular values used to describe the distribution of fault slip.

1987) and are a useful measure of change in the slip distribution as a function of added model terms. Model variances typically plateau for model terms greater than $k \sim 7$, indicating that the slip features specified by model terms $k < 7$ account for the majority of the roughness of the slip distribution.

Visual comparisons of the patterns of fault slip derived while employing different numbers of model terms indicate that the major features of the best-fitting slip models (Figs 10 and 11) are relatively insensitive to the number of model terms used to describe the pattern of slip, provided that the number of terms equals or exceeds that indicated above. Distributions of fault slip that employ only the lower-order model terms ($k < 7$) consist predominantly of one or two oval patches of fault slip that stand out from a noisy, low-slip-magnitude background. Slip distributions that incorporate additional higher-order model terms (those associated with singular values $k > 7$) exhibit additional higher wavelength, low-slip-magnitude patches of fault slip that do not significantly modify the positions or shapes of the major slip patches or their slip magnitudes. Based on these results, we employ nine singular values for March 1996–March 1997 and seven singular values for the remaining intervals to describe the best-fitting slip distributions.

6 DISTRIBUTIONS OF COSEISMIC AND POST-SEISMIC FAULT-SLIP

The best-fitting patterns of slip along the subduction interface for the coseismic and four post-seismic intervals are derived via SVD inversion of the GPS interval displacements (Table 2) and employ the preferred fault geometry and other parameters described in Section 5. Details of the best-fitting solutions and their fits to the data are shown in Figs 10 and 11 and are described in Sections 6.1–6.5. The effect of possible motion of the Jalisco Block on the estimated slip distributions is summarized in Section 6.6.

Table 2. GPS displacements and elastic model predictions: 1995–1999.

Site	North				East				Vertical			
	Measured	1σ	Pred.	Data Imp.*	Measured	1σ	Pred.	Data Imp.*	Measured	1σ	Pred.	Data Imp.*
	(millimeters)				(millimeters)				(millimeters)			
					Coseismic: March, 1995–October, 1995							
CRIP	−380.2	1.6	−380.3	0.998	−290.8	3.4	−290.0	0.976	−61.5	7.4	−59.9	0.924
CHAM	−843.2	3.5	−844.0	0.996	−476.3	8.7	−484.2	0.960	−214.6	17.4	−185.8	0.864
PURI	−411.7	4.0	−412.9	0.923	−273.0	8.9	−273.6	0.064	−101.6	19.8	−128.0	0.019
AVAL	−71.8	3.7	−77.4	0.059	−134.7	8.3	−122.5	0.017	−68.5	17.4	−14.3	0.001
AYUT	−176.0	6.5	−155.0	0.059	−129.0	13.3	−122.8	0.012	−163.6	33.0	−17.7	0.000
GUAC	−115.8	5.1	−112.5	0.051	−49.5	10.1	−77.1	0.007	−42.0	25.4	−7.8	0.000
CHAC	−87.9	4.7	−66.2	0.027	−26.4	10.8	−17.5	0.001	−8.0	25.3	−11.6	0.000
TAPA	−108.8	6.2	−96.2	0.022	−125.7	16.2	−112.7	0.004	−23.6	34.1	−6.0	0.000
SJDL	−1.0	3.8	−11.1	0.007	0.9	9.3	−29.6	0.002	−62.0	20.4	−22.0	0.000
CEBO	−30.5	5.6	−38.9	0.004	−60.3	11.4	−52.3	0.002	−15.0	26.1	1.6	0.000
VICT	9.4	3.4	−12.7	0.001	−23.0	7.8	−39.0	0.001	−60.6	16.4	−13.6	0.000
					October, 1995–March, 1996							
CRIP	−103.4	1.4	−103.6	0.998	−2.1	3.1	−2.8	0.978	97.4	6.9	100.3	0.920
CHAM	−75.6	2.9	−75.8	0.996	−51.6	6.3	−52.7	0.978	144.3	14.1	149.0	0.893
PURI	−108.3	3.7	−105.3	0.888	−53.2	7.0	−72.7	0.078	26.4	17.8	−45.3	0.018
AVAL	−29.9	3.2	−22.9	0.068	−15.1	7.0	−41.9	0.020	16.1	15.5	−9.7	0.001
AYUT	−65.7	5.1	−52.2	0.063	−7.1	9.7	−36.5	0.014	67.3	24.5	−11.5	0.001
GUAC	−49.5	4.6	−36.3	0.041	−13.1	8.5	−22.3	0.006	40.9	23.3	−5.2	0.000
TAPA	−42.9	6.3	−34.5	0.017	−51.5	16.0	−41.0	0.003	2.9	34.6	−8.1	0.000
CHAC	−20.6	4.0	−18.2	0.014	9.7	8.9	−5.9	0.000	−10.2	22.2	−7.2	0.000
CEBO	−19.4	5.5	−12.8	0.003	−13.3	9.8	−17.9	0.002	39.5	26.4	−0.8	0.000
SJDL	−6.8	3.5	—	—	7.1	8.1	—	—	14.8	18.3	—	—
VICT	−18.1	2.9	—	—	5.8	6.2	—	—	45.2	13.7	—	—
					March, 1996–February, 1997							
CRIP	−43.3	1.5	−44.1	0.988	−6.9	3.2	−13.1	0.914	−1.6	7.0	24.5	0.749
CHAM	−19.8	2.8	−21.9	0.967	−22.3	5.9	−28.3	0.811	33.9	13.2	98.4	0.489
MELA	−35.8	3.0	−37.3	0.941	−6.8	6.3	−13.2	0.499	16.6	14.4	97.3	0.154
TOMA	−16.5	3.6	−23.0	0.777	−27.5	7.4	−27.4	0.091	−40.6	16.4	8.2	0.020
GUFI	−32.3	3.1	−39.7	0.527	−29.2	7.9	−29.4	0.033	−2.5	14.4	−8.9	0.034
PURI	−47.5	3.4	−40.5	0.298	−23.6	7.4	−29.1	0.026	−29.7	15.9	−10.7	0.005
CHAC	−13.5	3.4	−14.9	0.165	−20.1	6.9	−6.0	0.006	−31.5	19.2	−4.7	0.000
AUTA	−41.6	3.4	−32.8	0.112	−23.4	7.9	−30.7	0.019	−17.4	16.2	−14.2	0.002
AYUT	−33.6	3.1	−26.5	0.104	−29.4	6.7	−20.7	0.024	−9.0	14.2	−7.5	0.001
GUAC	−35.1	3.0	−19.4	0.072	−22.4	6.4	−13.1	0.012	−23.2	14.6	−3.4	0.000
AVAL	−30.2	3.9	−10.8	0.047	−14.3	8.4	−18.3	0.012	−13.9	18.6	−4.8	0.001
CGUZ	−24.6	2.9	−8.2	0.033	−20.0	6.2	−13.3	0.009	−11.7	13.6	−2.1	0.000
UMON	−14.1	2.1	−7.6	0.020	−19.7	4.1	−7.3	0.005	−36.9	9.3	−0.2	0.000
COSA	−21.2	3.6	−7.6	0.009	−12.0	7.4	−9.3	0.002	−27.4	17.2	−0.6	0.000
LIMA	−16.1	4.3	−9.7	0.009	−11.6	8.7	−10.5	0.002	−20.8	19.7	−0.8	0.000
MCAB	−16.8	2.8	−6.6	0.009	−2.3	6.2	−5.4	0.001	−1.8	13.3	0.1	0.000
JARA	−5.3	2.8	−1.9	0.001	−8.0	6.2	−2.4	0.000	−30.1	13.0	0.2	0.000
SJDL	−9.1	3.6	—	—	18.8	7.9	—	—	−19.8	18.8	—	—
VICT	−7.1	4.0	—	—	16.5	9.0	—	—	−27.4	19.0	—	—
					February, 1997–March, 1998							
CRIP	−11.8	2.3	−12.5	0.975	3.7	4.6	5.1	0.799	16.8	10.8	8.9	0.444
MELA	−12.0	2.8	−12.5	0.951	4.1	5.7	−3.1	0.642	48.2	13.3	52.6	0.207
CHAM	−6.2	2.8	−5.7	0.942	−9.9	5.7	−24.7	0.317	13.9	13.3	26.5	0.133
GUFI	−19.2	2.8	−14.1	0.551	−8.5	5.7	−11.9	0.049	20.7	13.8	−1.9	0.040
PURI	−9.7	3.1	−15.9	0.312	−15.7	6.8	−11.8	0.026	37.0	14.9	−4.2	0.006
AUTA	−16.1	3.2	−13.1	0.138	−19.9	7.0	−12.3	0.022	17.1	15.5	−6.3	0.002
AYUT	−17.9	2.9	−9.8	0.100	−13.5	6.0	−6.4	0.013	−25.2	13.8	−2.7	0.001
AVAL	−2.4	3.8	−2.5	0.092	−0.9	7.8	−5.8	0.023	−18.2	18.0	−1.4	0.001
CGUZ	7.4	3.1	−2.3	0.054	−5.4	6.9	−4.4	0.012	−9.3	14.7	−0.7	0.000
GUAC	−10.6	2.8	−6.4	0.051	−18.5	5.5	−3.6	0.005	−18.3	13.3	−1.1	0.000
UMON	2.2	1.9	−2.5	0.030	1.5	3.9	−2.3	0.004	40.7	9.1	−0.1	0.000
COSA	−3.2	3.5	−2.4	0.015	−20.5	7.0	−3.1	0.003	21.2	17.0	−0.2	0.000
LIMA	−3.5	3.9	−3.2	0.015	−15.0	7.6	−3.5	0.003	12.5	17.8	−0.3	0.000
MCAB	−8.0	2.7	−2.1	0.009	−18.2	5.3	−1.6	0.001	9.4	12.6	0.0	0.000

Table 2. (*Continued.*)

Site	North				East				Vertical			
	Measured	1σ	Pred.	Data	Measured	1σ	Pred.	Data	Measured	1σ	Pred.	Data
	(millimeters)			Imp.*	(millimeters)			Imp.*	(millimeters)			Imp.*
CHAC	0.4	3.8	−2.4	0.008	6.8	7.3	−1.0	0.000	6.0	21.5	−0.9	0.000
JARA	−3.5	2.6	−0.6	0.001	−6.5	5.4	−0.7	0.000	−0.4	12.5	0.1	0.000
SJDL	8.5	3.5	—	—	−3.9	7.1	—	—	17.7	20.0	—	—
VICT	5.0	4.0	—	—	−16.3	9.0	—	—	−7.6	19.6	—	—
					March, 1998–March, 1999							
CRIP	1.6	2.0	−0.2	0.973	−2.4	4.1	2.9	0.529	−6.7	9.7	−3.6	0.217
MELA	3.6	2.4	1.5	0.941	10.0	4.8	6.1	0.655	14.2	12.1	37.4	0.174
CHAM	−3.8	2.5	−3.3	0.932	4.1	4.9	−14.3	0.277	23.0	12.2	13.7	0.114
GUFI	−19.7	2.5	−15.5	0.506	−1.1	4.8	−11.0	0.049	7.6	12.2	−14.6	0.041
COOB	1.9	1.1	−0.8	0.428	0.4	2.1	−2.3	0.128	11.8	5.0	−0.1	0.008
PURI	−14.6	2.6	−16.1	0.339	8.7	4.8	−9.1	0.035	6.5	12.4	−8.5	0.007
AUTA	−15.7	2.5	−7.9	0.136	2.9	5.0	−8.0	0.030	0.0	12.1	−2.6	0.003
AYUT	−15.1	2.5	−4.9	0.089	6.1	4.8	−3.8	0.015	25.0	12.4	−0.8	0.001
AVAL	0.7	2.7	−0.9	0.072	−2.0	5.0	−2.4	0.019	27.1	12.6	0.0	0.001
TAPA	−1.1	2.5	−1.6	0.062	−6.6	5.2	−2.8	0.013	21.6	12.8	0.1	0.001
GUAC	−9.7	2.4	−3.2	0.048	−2.5	4.6	−2.1	0.006	24.2	11.8	−0.3	0.000
UGEO	−1.7	1.2	−0.9	0.033	−8.3	2.4	−1.0	0.006	7.9	5.8	0.1	0.000
CGUZ	−5.4	2.9	−0.7	0.022	−5.2	6.5	−1.5	0.005	6.5	13.8	0.1	0.000
SEBA	−14.2	3.3	−2.7	0.017	8.3	6.3	−0.9	0.001	0.8	17.6	−0.4	0.000
LIM2	−13.7	2.7	−1.1	0.014	−3.4	5.2	−1.5	0.003	20.8	12.8	0.1	0.000
CEBO	−3.4	2.6	−0.6	0.009	−5.9	5.4	−1.1	0.003	−1.2	12.8	0.1	0.000
COSA	−7.3	2.8	−0.8	0.009	−1.1	5.1	−1.2	0.003	18.1	13.3	0.1	0.000
UMON	−13.6	2.5	−1.0	0.008	−7.0	5.2	−1.1	0.001	−24.8	12.2	0.1	0.000
CHAC	−8.3	3.4	−1.9	0.007	2.5	6.4	−0.6	0.000	6.6	19.2	−0.5	0.000
MCAB	3.1	2.4	−0.9	0.006	10.2	4.7	−0.8	0.001	10.9	12.0	0.1	0.000
JARA	1.3	2.4	−0.2	0.001	6.7	4.8	−0.3	0.000	21.3	11.8	0.0	0.000
SJDL	7.6	3.3	—	—	22.7	6.8	—	—	28.8	19.3	—	—
VICT	2.5	2.6	—	—	22.5	5.2	—	—	12.9	13.1	—	—

*—Data importance. Data are listed in descending order of the data importance for the north component. Displacements are relative to North American Plate as defined in text. Displacement uncertainties are propagated from GPS data noise, daily location repeatabilities, and the angular velocity that describes motion of the North American Plate relative to ITRF97. Predictions are from best-fitting elastic half-space models described in text.

Table 3. Characteristics of candidate fault-slip solutions.

Term	3/95–10/95		10/95–3/96		3/96–2/97		2/97–3/98		3/98–3/99	
	SNR[1]	Model variance	SNR	Model variance	SNR	Model variance	SNR	Model variance	SNR	Model variance
1	264.3	404254	75.2	25184	37.3	6597	11.3	971	5.3	150
2	257.3	1709373	28.9	36439	14.2	8694	0.1	971	2.5	212
3	11.7	1715256	16.1	45625	1.9	8754	0.3	972	0.5	215
4	5.7	1716973	18.6	61297	13.5	14958	7.5	3136	5.7	967
5	47.0	1941729	21.2	95338	2.4	15200	2.9	3606	8.0	2984
6	10.2	1964768	14.5	122564	9.0	18817	2.2	3913	1.9	3128
7	27.5	2165014	7.4	132484	4.3	19793	0.1	3914	0.8	3160
8	4.8	2172193	0.0	132484	4.6	21396	2.9	4817	5.9	5815
9	0.5	2172452	4.5	146076	6.5	25855	3.1	6419	3.1	6955
10	3.0	2183940	1.0	147039	2.5	27080	1.8	7075	3.8	9134
11	3.2	2204565	0.5	147380	0.8	27239	0.4	7112	0.5	9181
12	0.7	2208134	4.1	234884	1.2	27555	1.5	7934	3.2	11662

1—SNR represents the magnitude of the model term divided by its formal uncertainty. Model variance represents the length of the solution vector and measures the roughness of the slip distribution. Data variance as a function of model terms is shown in Figure 9.
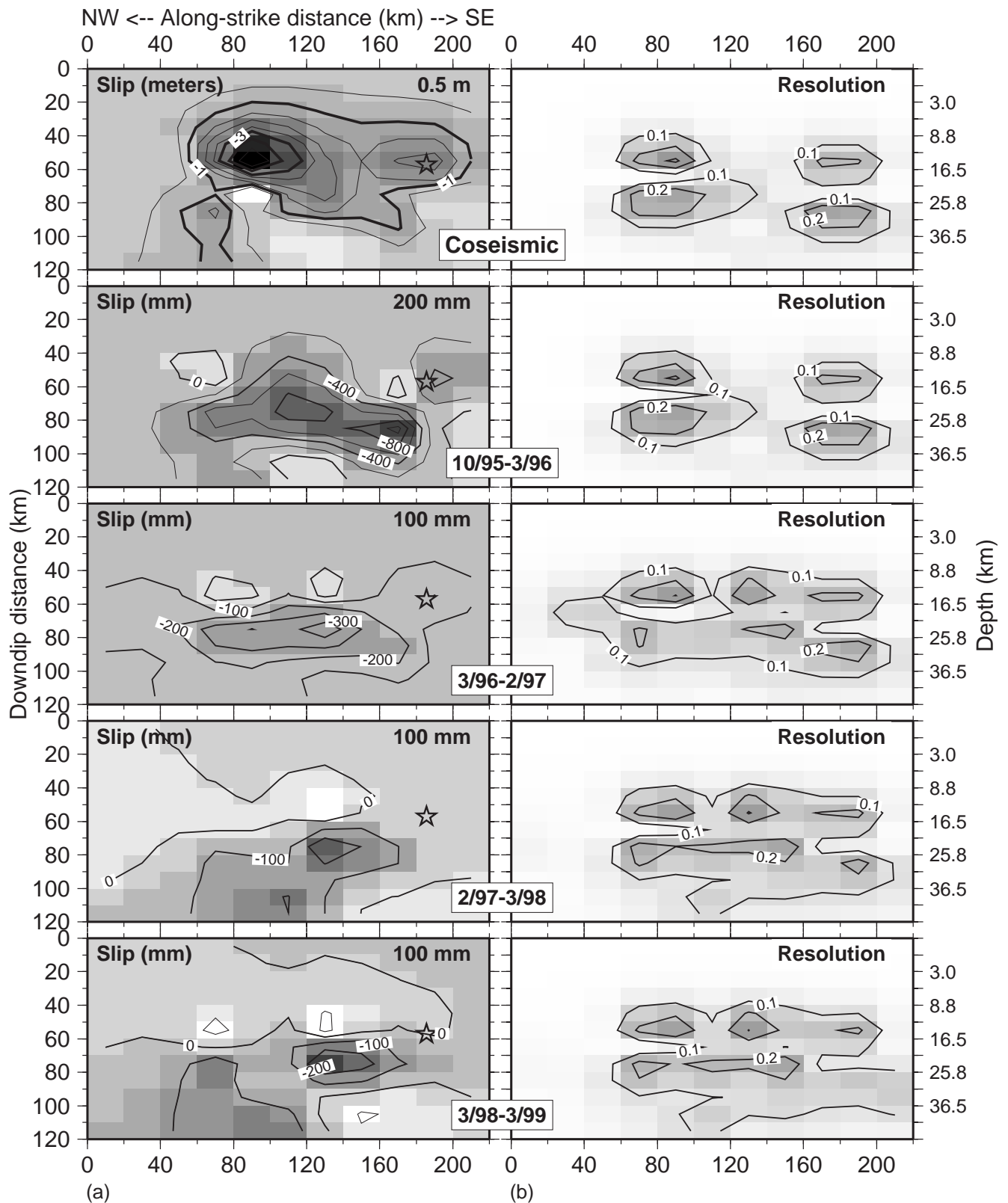
Figure 10. (a) Best-fitting distributions of slip along subduction interface for coseismic and post-seismic intervals. Fits to vertical and horizontal displacements are shown in Figs 7 and 11, respectively. Negative slip denotes downdip motion of the subducting slab, representing strain release. Positive slip denotes locked areas of the subduction interface. Along-strike and downdip distances are measured from the intersection of the northwest corner of the fault with the surface (see also Fig. 11). Contour intervals in metres or millimetres are given by numbers in upper right-hand corners. Star is projection of the 1995 October 9 earthquake epicentre onto the fault. (b) Formal resolution of fault slip shows areas of the fault where slip is better resolved (dark shades) or poorly resolved (light shades).
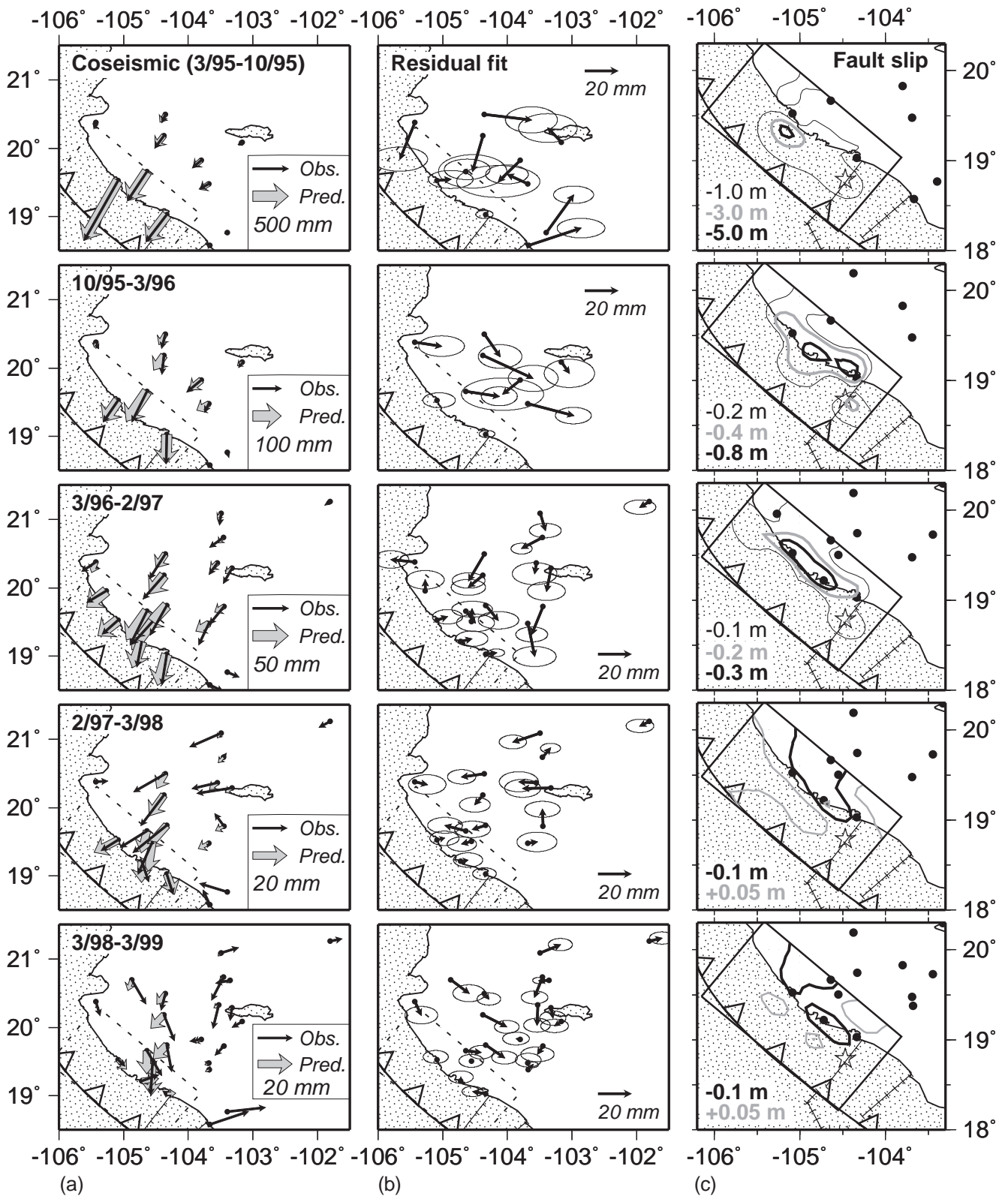
Figure 11. (a) Observed (solid arrows) and predicted (shaded arrows) geodetic displacements for a given interval. Predicted displacements are for the best-fitting slip distributions shown in Fig. 10. (b) Residual fits to geodetic displacements shown in leftmost column. Predicted displacements are subtracted from the observed displacements. Ellipses are the 2-D, 1σ observation uncertainties. Dashed lines show the surface projection of the curved fault used to fit the data. (c) Spatial evolution of fault slip from March 1995–March 1999. Slip contours from Fig. 10 are projected to the surface. Star shows 1995 October 9 epicentre from Pacheco *et al.* (1997). Circles show the locations of GPS displacements used to constrain the slip for a given interval.

6.1 Coseismic: March–October, 1995

GPS measurements in March and mid-October of 1995 at the eleven sites that comprised our geodetic network at the time provide our best estimate of the coseismic response of the 1995 October 9 earthquake. Although we refer to these as the coseismic displacements, they also include seven months of presumed slow strain accumulation prior to the earthquake and six or more days of afterslip.

The pattern of coseismic slip that best fits these displacements (Fig. 10) strongly resembles that derived in our earlier study (Melbourne *et al.* 1997), even though our earlier study assumed a suboptimal, planar fault geometry. Most of the coseismic moment appears to have been released in two locations: near the earthquake epicentre (i.e. immediately northwest of the Manzanillo Trough), where 1–2 m of slip occurred, and ~100 km northwest of the epicentre, where 4–5 m of slip occurred. Slip in both locations was largely focused above depths of 21 km.

The geodetically-constrained pattern of coseismic slip is broadly similar to a slip distribution constrained by inversion of broadband teleseismic *P* waves (Mendoza & Hartzell 1999). Both suggest that 1.5–2.0 m of slip occurred in the vicinity of the earthquake epicentre and both include a more extensive zone of slip ~80–120 km to the northwest of the epicentre (Fig. 10). The geodetic observations however suggest that most of the slip in the latter region was focused approximately 30–60 km downdip, at depths of 6–20 km, whereas the seismologic data suggest that slip was focused principally from 0–30 km downdip at depths of 3–13 km. The apparent lack of near-surface slip in the geodetically-constrained slip model may stem from the fact that the geodetic observations are relatively incapable of resolving near-surface fault slip (see Fig. 10b) due to their distance from the shallowest parts of the fault.

The coseismic slip distribution also includes a zone of slip between, but 10–20 km downdip from the two main rupture patches (Fig. 10). Continuous GPS measurements at site CRIP beginning 6 days after the earthquake require that at least some (or possibly all) of this deeper slip occurred after the earthquake. These measurements show that CRIP was already undergoing continuous uplift 6 days after the earthquake, the opposite of its coseismic vertical motion (Melbourne 1998).

The reversal in the sense of the vertical motion at CRIP is consistent with a post-seismic downdip migration of fault slip that caused a landward shift of the hinge line that separated regions of elastically-induced subsidence and uplift. The pattern of coseismic slip shown in Figs 10 and 11 is thus a hybrid of shallow coseismic slip and at least some deeper post-seismic slip.

The earthquake moment of the geodetically-constrained slip model is $7.5 \cdot 10^{20}$ N·m, assuming a standard value of 30 GPa for the shear modulus. Patches of negative fault slip, which represent downward-directed dip-slip motion of the subducting plate, account for 95 per cent of the geodetic moment. The small patch of positive slip located below the main rupture zone (Fig. 10) is likely a modelling artifact. Moments estimated from seismologic data are $1.2 \cdot 10^{21}$ N·m (Dziewonski *et al.* 1997), $8.3 \cdot 10^{20}$ N·m (Mendoza & Hartzell 1999) and $1.8 \cdot 10^{20}$ N·m (Escobedo *et al.* 1998). The geodetically-constrained moment thus lies near the midpoint of the seismologic estimates, but includes a contribution from an unknown amount of post-seismic slip.

Relative to the cumulative data importance of 7.0 (equaling the number of singular values that are used to generate the slip distribution), the horizontal and vertical displacements at coastal sites CRIP and CHAM have summed importances of 5.7 (Table 2) and thus provide more than 80 per cent of the information that constrains the coseismic slip distribution. Their high cumulative importance demonstrates that the model is constrained largely by the displacements of the coastal sites and also explains why the coastal displacements for this and the other intervals we modelled are typically fitted better than displacements from sites farther inboard (Figs 7 and 11). Numerical experiments show that the proximity of the coastal sites to the subduction interface is the most important factor in determining their high data importance.

The reduced chi-square (χ_v^2) is 6.4 for the best-fitting coseismic slip model (Table 4), indicating that the average misfit of 10–20 mm in the horizontal and 30–50 mm in the vertical exceeds the average uncertainty by a factor of 2.5. Since we believe the estimated displacement uncertainties are approximately correct (see Section 3.3), the larger-than-expected misfits may result from the simplistic assumption that all of the coseismic surface deformation represents a homogeneous

Table 4. Model fits, data importances, and moment release.

Interval	$\chi_v^{2\,1}$	DOF	Data importance			Summed Importance	Slip moment[2]
			North	East	Vertical		
3/95–10/95	6.39	26	3.15	2.05	1.81	7.00	$7.5 \cdot 10^{20}$**
10/95–3/96	4.84	20	3.09	2.08	1.83	7.00	$1.9 \cdot 10^{20}$
96–97	6.83	42	5.08	2.47	1.46	9.00	$9.1 \cdot 10^{19}$
97–98	3.04	41	4.25	1.92	0.83	7.00	$2.9 \cdot 10^{19}$
98–99	4.18	56	4.65	1.78	0.57	7.00	$2.4 \cdot 10^{19}$

1—χ_v^2 is reduced chi-square, the weighted least-squares misfit of the best-fitting elastic model divided by the degrees of freedom (DOF) for that model. The degrees of freedom for a given model equals N-7 or N-9, where N is the number of data used to derive the model and either seven or nine singular values are used to fit the data depending on the interval (see text).

2—Slip moments are in units of Newton metres.

**—We estimate that 85 percent ($6.4 \cdot 10^{20}$ N·m) of the slip moment occurred during the earthquake and the remaining 15 per cent during the six days after the earthquake before we were able to reoccupy the GPS network. Details are given in Section 7.2.

elastic response to slip along the subduction interface. Similar-sized and even larger misfits to the GPS displacements reported by Klotz *et al.* (1999) for the 1995 Antofagasta subduction earthquake ($M_w = 8.0$) along the Peru–Chile trench lend support to this interpretation.

6.2 Postseismic: October, 1995–March, 1996

Inversion of the nine displacements for sites occupied in October 1995 and March 1996 yield average misfits that improve slightly ($\chi^2_v = 4.8$) relative to the previous interval. The model correctly reproduces the general pattern of southwest-directed horizontal motion (Fig. 11 and Table 2) and also correctly predicts uplift along the coast (Fig. 7). The displacements of the sites inboard from the coast are fitted more poorly than the high-importance displacements at CRIP and CHAM (Fig. 11). Moreover, the model fails to predict the uplift observed at sites inboard from the coast. An elastic model that predicts uplift at the inboard sites would require the existence of afterslip at implausible depths given the steep dip of the Benioff zone. We thus suspect that the uplift is caused by some other mechanism such as viscoelastic rebound or transient fluid flow in the upper crust.

Although shallow afterslip is observed in the vicinity of the earthquake epicentre and offshore from site CHAM, most post-seismic slip during this interval shifted ~ 20–40 km down the subduction interface relative to the locus of coseismic slip (Fig. 10). Nearly 70 percent of the slip moment of $1.9 \cdot 10^{20}$ N·m for this period was concentrated beneath depths of 16 km, whereas 70 percent of the coseismic moment release occurred above depths of 21 km. A comparison to the relatively shallow-focus coseismic slip distribution derived from seismic data (Mendoza & Hartzell 1999) further reinforces the evidence that slip migrated to deeper regions of the subduction interface after the earthquake.

6.3 Postseismic: March, 1996–February, 1997

New coastal and inboard sites that were installed and occupied in March 1996 significantly improved the network geometry relative to the two previous intervals, thereby partially off-setting the imbalance of model information supplied by the coastal sites during the two previous intervals. Inversion of the displacements for 17 sites that were occupied in March 1996 and February 1997 indicate that most afterslip remained focused along the subduction interface directly beneath the coastline (Fig. 10). Shallow afterslip offshore from CHAM, prominent during the previous interval, had ceased by March 1996, leaving only deeper slip in this region of the fault. Postseismic slip in the shallower levels of the subduction interface thus largely ceased within one year of the main shock. Two-thirds of the total slip moment for this interval ($0.9 \cdot 10^{20}$ N·m) was focused beneath depths of 16 km.

A second notable change is the apparent onset of downdip slip along the northwestern end of the subduction interface (Fig. 10), where no coseismic slip or earthquake aftershocks occurred (Pacheco *et al.* 1997; Mendoza & Hartzell 1999). Downdip slip along this part of the subduction interface is required to fit the displacements of the nearby sites TOMA and CHAC, which moved down and to the southwest during this interval (Figs 7 and 11). The summed moment for the fault elements that comprise this part of the subduction interface

is $\sim 1 \cdot 10^{19}$ N·m, equal to that released by more than 1000 hypothetical earthquakes of $M_s = 4.5$. Given that no earthquakes above $M_s = 4.0$ were reported by the Mexican National Seismic Service during this period for this section of the trench and that coseismic slip did not extend this far to the northwest, we speculate that a slow rupture or extended period of aseismic creep occurred somewhere northwest of site CHAM during this 1 yr period.

Misfits to the March 1996–February 1997 displacements (Fig. 11) display two distinct patterns—horizontal components of displacements of sites located inboard from the coast are systematically overestimated and the model predicts significantly more uplift along the coast and significantly less uplift at inboard sites than observed (Fig. 7). The tendency for the model to preferentially misfit displacements at the inboard sites stems from the previously described imbalance in the information content of the data—displacements for the coastal sites CRIP, CHAM, and MELA constrain 6.5 of the nine singular values and are hence better fit than are displacements at the remaining sites (Fig. 11).

Many of the residual displacement vectors for this interval (Fig. 11) and the displacements at SJDL and VICT (Fig. 5) point to the southeast toward the epicentre of the 1997 January 11 ($M_w = 7.2$) earthquake that ruptured the Cocos subduction interface ~ 100 km southeast of the network. We extended the subduction interface farther to the southeast to allow for the possibility of coseismic slip release associated with this earthquake; however, this did not significantly reduce χ^2_v (Table 4).

6.4 Postseismic: February, 1997–March, 1998

Despite the smaller signal-to-noise ratio for displacements for February 1997–March 1998, the horizontal displacements are remarkably coherent and with few exceptions point toward the coast. Vertical displacements display a pattern similar to that shown during the previous year, with uplift along the coast and slow subsidence at many sites farther inboard (Fig. 7). SVD inversion of the 16 displacements for this period (excluding SJDL and VICT) indicates that slip along the subduction interface remained focused beneath the coast at a depth of 18–33 km (Figs 10 and 11), with the principal difference being the 70 per cent decrease in the slip moment (Table 4).

Relative to previous intervals, the horizontal and vertical displacements are better fit, with $\chi^2_v = 3.0$ (Table 4). The improvement in fit is due in part to the decreased signal-to-noise ratio. Displacements of the coastal sites, which have high data importances, are well fit (Figs 7 and 11), whereas the coastward displacements for most sites farther inland are underestimated and thus have residual displacements that point toward the coast (Fig. 11). As discussed in Section 8, the spatial coherence of the residual displacements suggests that unmodelled processes contribute significantly to post-seismic slip or that spatially-correlated errors exist in the GPS displacements.

Unlike previous intervals, limited zones of positive slip, representing locked patches of the subduction interface, occur above depths of 16 km (Fig. 10). The seismic moment deficit implied by these patches equals only 5 percent of the overall slip moment for this interval. Although these may be artifacts of the modelling, they resemble smaller, identically positioned patches of positive slip from the previous interval (March 1996–February 1997) and more extensive, similarly positioned zones of positive slip for March 1998–March 1999. The persistence

and expansion of the zones of positive slip after March 1996 suggests that the limited regions of apparent strain accumulation during February 1997–March 1998 represent relocking of the shallow subduction interface that may have started as early as March 1996.

6.5 Postseismic: March, 1998–March, 1999

The pattern of fault slip that best fits displacements of the 21 sites occupied in March 1998 and 1999 (Figs 10 and 11) strongly resembles that for the previous interval. Downdip slip, representing afterslip, remained stationary with respect to afterslip from February 1997–March 1998 (Fig. 10) and decayed to 65 percent of the afterslip moment for February 1997–March 1998. The area of shallow strain accumulation expanded significantly, with a slip moment deficit ∼4 times greater than for the previous interval. Numerical experiments indicate that the combination of afterslip at depths below 16 km and strain accumulation along the shallow part of the subduction interface is a persistent feature of the fault slip for this period.

Although most vertical displacements during this period indicate slow regional uplift (Table 2 and Fig. 7), the model predicts there was little or no vertical motion except at coastal sites CHAM and MELA. This continues a pattern of misfits to the vertical displacements at inboard sites for previous intervals and suggests that different modelling assumptions are needed such as allowing for a viscoelastic response.

6.6 Effects of potential Jalisco Block motion

Motion of the Jalisco Block relative to the North American Plate has occurred since 5 Ma along faults in the Colima Graben and Tepic–Zacoalco Fault zone and may still occur today. Geologic evidence suggests that any such block motion is slower than several millimetres per year (see Section 2) and thus contributes marginally to the rapid displacements before February 1997 (Figs 5 and 11). For later times, block motion of several millimetres per year would constitute a more significant fraction of the displacements measured for the 12 sites located on the Jalisco Block.

We thus tested how unmodelled Jalisco Block motion might affect the slip distributions for February 1997–March 1998 and March 1998–March 1999 by assuming two models that bracket the range of geologically plausible models for the present motion of the Jalisco Block relative to North America. In one model, we assume that the Jalisco Block moves 3 mm yr^{-1} to the southwest relative to North America, corresponding to oblique opening across the Tepic–Zacoalco Fault zone and Colima Graben. In the second, we assume that block motion is 3 mm yr^{-1} to the northwest, implying pure opening across the Colima Graben and dextral strike-slip along the Tepic–Zacoalco Fault zone. These rates exceed geologically-based estimates for these features (Allan 1986; Ferrari *et al.* 1994) and thus maximize the effect of Jalisco Block motion on our results.

Inversions of the observed GPS displacements for February 1997–March 1998 and March 1998–March 1999 after correcting the motions of the Jalisco Block sites for assumed southwestward motion of the Jalisco Block yields slip distributions that closely resemble those derived from the unmodified displacements (Fig. 10). The modified slip distributions consist of oval-shaped patches of downdip slip below depths of 16 km

and patches of strain accumulation at depths shallower than 16 km. Repeating this exercise while assuming northwestward translation of the Jalisco Block sites relative to North America also yields patterns of fault slip that differ negligibly from their best-fitting counterparts.

We conclude that the best-fitting patterns of fault slip are insensitive to slow, unmodelled translation of the Jalisco Block sites. We did not attempt to test the potential effect of slow rotation of the Jalisco Block about a nearby vertical axis, primarily because the result would depend strongly on the location we assumed for the rotation axis.

7 SPATIO-TEMPORAL EVOLUTION OF POST-SEISMIC SLIP

7.1 Testing for spatial variations in the fault-slip distribution

The lack of reliable uncertainties associated with the distributions of fault slip shown in Fig. 10 make it difficult or impossible to determine whether the pattern of slip along the subduction interface changes significantly through time. We thus employ the procedure described in Section 4.2 to search for such differences, allowing only for a scale difference in slip magnitudes from one interval to the next.

We first tested our procedure on two slip distributions that almost certainly differ from each other, namely, those for the interval spanning the earthquake (March 1995–October 1995) and the first post-seismic interval (October 1995–March 1996). The least-squares misfit χ^2 for the stationary-slip model, which employs seven singular values and a linear scaling constant to fit the combined displacements for these intervals, is 2336.0 (Table 5). Chi-squared for the corresponding best-fitting slip distributions, each of which employs seven singular values, is 263.0. The fit for the latter model thus improves on that of the former by a factor of 9 (Table 5). A comparison of the fits for the two models using an F-ratio test for six additional model

Table 5. Test for significant spatial variations in fault-slip.

Interval	χ^2*		Number of data	Probability[1]
	Best	Combined		
Two-interval tests: 3/95–3/99				
3/95–10/95–3/96	263.0	2336.0	60	$4 \cdot 10^{-20}$
10/95–3/96–97	446.5	557.6	78	0.02
96–97–98	474.1	490.1	99	0.82
97–98–99	358.5	390.2	111	0.21
Three-interval test: 3/96–3/99				
96–97–98–99	708.1	784.0	162	0.25

*χ^2 is the weighted least-squares misfit of the model to the combined data for the listed intervals. Two-interval tests employ 14 adjustable parameters for the best fitting model and eight parameters for the combined model (see Section 4.2). Three-interval test employs 21 adjustable parameters for the best-fitting model and nine parameters for the combined model.
1—The probability is computed using the F-ratio test for additional model terms (Bevington & Robinson 1992). Probability expresses the likelihood that the improvement in fit of the best-fitting model relative to the combined-fit model is merely a random outcome of fitting the data with additional adjustable parameters. Probability values smaller than 0.05 indicate that the model fits differ at more than the 95 percent confidence level.

terms shows that they differ at very high confidence levels (4 parts in 10^{20}). The slip patterns for these two intervals thus differ significantly, implying that the downdip migration of slip after the earthquake (Fig. 10 and 11) is strongly required.

A comparison of the best fitting and stationary-slip models for the intervals October 1995–March 1996 and March 1996–February 1997 (Table 5) shows that they also differ at more than the 95 percent confidence level, presumably reflecting the cessation of shallow afterslip offshore from site CHAM (Fig. 10). The best-fitting models for intervals later than March 1996 do not significantly improve on stationary-slip models for those intervals (Table 5), indicating that there were no significant changes in the pattern of afterslip after March 1996. To further test this result, we simultaneously fit the displacements for the final three post-seismic intervals while using seven singular values and two adjustable constants to scale the displacements for the February 1997–March 1998 and March 1998–March 1999 intervals relative to the displacements for March 1996–February 1997. The summed fits of the three best-fitting slip distributions fail to improve significantly on that of the simpler stationary-slip model, thereby underscoring that the pattern of slip did not change significantly from March 1996 to March 1999.

7.2 Temporal evolution of post-seismic slip

We next fit the horizontal displacements for the eight sites with the longest time series and highest signal-to-noise ratios (Fig. 12) to test whether the observed post-seismic transients are consistent with a prediction of the rate- and state-variable friction model, namely, that the post-seismic relaxation of frictional forces within velocity-strengthening areas of the subduction interface gives rise to a logarithmically-decaying post-seismic transient (Scholz 1990), provided that the locus of post-seismic slip is approximately stationary. Except for the cessation of a limited region of shallow afterslip located above depths of 20 km after March 1996 (Fig. 11), post-seismic slip has to first-order been focused beneath the coastline since the earthquake. We thus approximate the displacement time series for these eight sites using $u(t) = S_1 + A^* \ln(bt + 1)$, where $u(t)$ represents the post-seismic horizontal displacements of a given site, S_1 is the unknown amount of post-seismic motion of a site before it was first reoccupied after the earthquake, A is the site-specific amplitude of the post-seismic response, and b is the common time constant of decaying afterslip along the subduction interface (Marone *et al.* 1991).

Minimization of the least-squares difference between the observed displacements $u(t)$ at all eight sites and the above model yields good fits (Fig. 12) to their displacement time series, with $\chi_v^2 = 0.3$. The horizontal displacements are thus consistent with one prediction of the rate- and state-variable friction model. We did not try to fit the most recent displacements at sites CRIP and CHAM due to evidence described above for significant shallow strain accumulation that contaminates estimates of post-seismic afterslip at these sites.

The least-squares fit is optimized for decay constants b of 100–150. Half of the first year's post-seismic slip thus occurred within 30–40 days of the earthquake and half of the cumulative post-seismic slip occurred within 65–80 days. Values of S_1 range from 3 to 23 percent of the coseismic displacements and average ~15 percent, constituting our best estimate of how

much post-seismic slip contaminates the 'coseismic' displacements we measured one week after the earthquake. Assuming that the coseismic and post-seismic fractions of the slip moment for the period March 1995–October 1995 are ~85 percent (6.4×10^{20} N m) and ~15 percent (1.1×10^{20} N m), the adjusted slip moment for the post-seismic period October 1995–March 1999 then equals ~70 percent of the adjusted coseismic moment.

8 DISCUSSION AND CONCLUSIONS

Modelling of the coseismic and post-seismic surface displacements associated with the Colima–Jalisco earthquake suggests that coseismic slip was limited largely to areas of the subduction interface shallower than depths of ~20 km. In contrast, significant post-seismic slip was focused from depths of ~16–33 km (Figs 10 and 11) and continued at measurable levels for at least 3.5 years after the earthquake. Lesser afterslip occurred above depths of ~20 km at the location of the earthquake epicentre and offshore from site CHAM, but ceased within 1.5 years of the earthquake. Shallow post-seismic slip also appears to have occurred significantly northwest of the coseismic rupture zone during March 1996–February 1997 (Fig. 10), along a previously inactive area of the subduction interface. No significant earthquakes were recorded during this period for this part of the subduction interface, suggesting that the geodetically-recorded surface displacements captured an aseismic slip event near the northwestern end of the trench.

The pattern of fault slip since March 1996 also includes increasingly extensive areas of shallow strain accumulation. Slip indicative of strain accumulation during February 1997–March 1998 and March 1998–March 1999 accounted for 5 per cent and 23 percent of the respective moment releases for these periods, strongly suggesting increased frictional relocking of the shallow subduction interface. The co-existence of deep afterslip and a locked upper fault implies extension within the subducting slab, compression within the upper plate, or some combination thereof.

Interpreted in the context of a rate- and state-variable friction model (Dieterich 1979; Ruina 1983, Scholz 1990; Scholz 1998), the difference in the durations of afterslip along the subduction interface above and below depths of 16–20 km implies that different frictional stability regimes apply in these regions. Coseismic rupture of several metres along the shallow part of the subduction interface and the relative absence of shallow afterslip indicate that the materials lining this part of the interface exhibited a velocity-weakening and hence friction-reducing response to the sudden increase in the local fault-sliding velocity, thereby creating the dynamic instability that propagated the rupture. By implication, this part of the interface is strongly coupled between earthquakes.

The relative lack of coseismic slip below depths of ~20 km and the strong evidence for decaying afterslip imply that the materials lining this part of the interface are velocity-strengthening. They responded to the coseismic rupture via a short-term increase in the local frictional forces, thereby arresting its advance and causing an increase in the ambient stress along the velocity-strengthening areas of the fault. This in turn induced logarithmic decay of the frictional forces along the downdip regions of the fault, which resulted in afterslip that gradually reduced the locally-elevated ambient stress to the static strength of the fault.
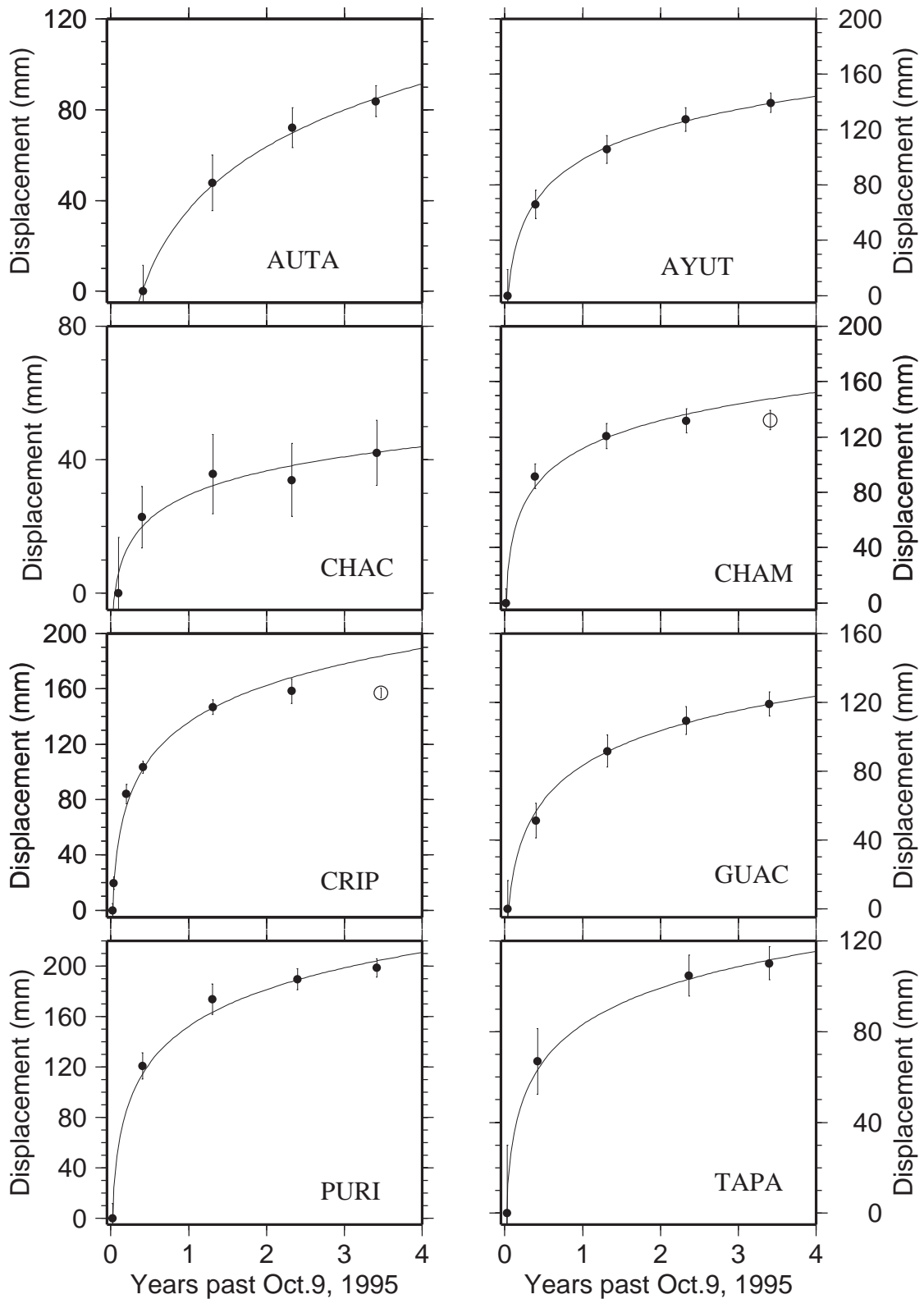
Figure 12. Observed horizontal displacements for selected sites (circles) and best-fitting logarithmic decay models. Error bars are standard errors. Displacements are measured relative to the location of a site when it was first occupied after the 1995 October 9 earthquake. Open circles depict data that are not used for reasons described in the text.

The patterns of coseismic and post-seismic fault slip for the Colima–Jalisco earthquake differ significantly from results reported by Heki *et al.* (1997) for the 1994 December 28 ($M_w = 7.6$) interplate thrust earthquake along the Japan trench.

Afterslip associated with this earthquake occurred over a broad area that included the coseismic rupture zone and adjacent areas of the subduction interface. The geodetic displacements showed no evidence of downdip migration of afterslip, thereby

indicating that afterslip was limited primarily to the shallow portions of the subduction interface. Heki *et al.* (1997) suggest that the observed distribution of afterslip is consistent with that expected for a subduction interface with significant, shallow-depth, velocity-strengthening regions (i.e. regions where inter-seismic creep occurs). Their results thus conform to *a priori* expectations for the Japan trench, which exhibits a long-term seismic moment deficit indicative of a partially coupled sub-duction interface (Pacheco *et al.*, 1993). The differences in the post-seismic distributions of afterslip for the Colima–Jalisco and Japan trench earthquakes presumably reflect the difference between a strongly coupled and partially coupled subduction interface.

The ~ 20 km depth limit to the zone of coseismic rupture is comparable to the ~ 20–25 km depth limit for the seismogenic zone estimated for the remainder of the Middle America Trench (Pacheco *et al.* 1993; Pardo & Suárez 1995; Suárez & Sánchez 1996), but is less than half the maximum depth estimated for strong seismogenic coupling along most other subduction zones (Pacheco *et al.* 1993). The relatively shallow transition from the zone of unstable to stable frictional sliding for the Rivera subduction interface may result from a combination of the young age of the subducting plate (10 Ma), its slow conver-gence rate (~ 25–35 mm yr^{-1}), and its shallow slab dip ($15°$). Modelling of the thermal structure of the Cascadia subduction zone (Hyndman & Wang 1993), where 8 Myr seafloor subducts at a rate of 45 mm yr^{-1} at a 5–$15°$ dip, yields a transition depth of 20 km or shallower, suggesting a similarly shallow depth for the Rivera Plate.

A reliable estimate of the maximum depth and approximate dip of the seismogenic zone leads to a useful estimate of the maximum potential earthquake for the Rivera subduction zone. If the entire subduction interface ruptured from the surface to a depth of 16 km along the 300 km length of the trench northwest of the Manzanillo trough, the predicted moment magnitude would be 8.1–8.3 assuming average coseismic slip of 3–5 metres and a value of 30 GPa for the shear modulus. If the shallow subduction interface is fully locked (or nearly so), the present average convergence rate of 30 mm yr^{-1} implies an approximate recurrence interval of 100 years for the maximum moment earthquake. For comparison, three large-moment earth-quakes ruptured the Rivera subduction interface during the twentieth century, the $M_w = 8.0$ and 7.9 earthquakes of 1932 June 5 and 1932 June 18 (Singh *et al.* 1985), and the $M_w = 8.0$ earthquake of 1995 October 9.

Although the modelling results are consistent with the assumption that much of the post-seismic surface deformation represents a response to fault afterslip dictated by rate- and state-variable friction laws, the misfits of the simple elastic models to the coseismic and post-seismic displacements signifi-cantly exceed their average uncertainties for all intervals we modelled. We are now examining whether the displacements are fit equally well or better if we allow for viscoelastic responses of the lower crust and upper mantle and a transient poroelastic response of the upper crust (although neither can be invoked to explain the misfit to the coseismic displacements). Unmodelled slip along faults in the upper plate and/or heterogeneities in the elastic properties of the crust may instead be responsible for our inability to fit the coseismic and possibly post-seismic observations within their uncertainties. We also cannot exclude the possibility that we have underestimated the uncertainties in the displacements. Given that the random noise over several-

day periods is both well characterized and consistent with the levels of white noise reported elsewhere (see Section 3.3), this would imply that the displacement time series are contaminated by long-period noise.

REFERENCES

Allan, J.F., 1986. Geology of the northern Colima and Zacoalco grabens, southwest Mexico: late Cenozoic rifting in the Mexican volcanic belt, *Bull. geol. Soc. Am.,* **97,** 473–485.

Allan, J.F., Nelson, S.A., Luhr, J.F., Carmichael, I.S.E., Wopmat, M., Wallace, P.J., 1991. Pliocene-Holocene rifting and associated volcanism in southwest Mexico: An exotic terrane in the making, in *The Gulf and Peninsular Province of the Californias, AAPG Memoir,* **47,** pp. 425–445, eds Dauphin, J.P. & Simoneit, B.R.T., AAPG, Boulder.

Bandy, W., Mortera-Gutierrez, C., Urrutia-Fucugauchi, J., Hilde, T.W.C., 1995. The subducted Rivera–Cocos Plate boundary: Where is it, what is it, and what is its relationship to the Colima Rift?, *Geophys. Res. Lett.,* **22,** 3075–3078.

Bevington, P.R., Robinson, D.K., 1992. *Data reduction and error analysis for the physical sciences,* McGraw-Hill, New York.

Boucher, C., Altamimi, Z., Sillard, P., 1999. The 1997 International Terrestrial Reference Frame (ITRF97), *IERS Technical Note,* **27,** Observatoire de Paris.

Courboulex, F., Singh, S.K., Pacheco, J.F., Ammon, C.J., 1997. The October 9, 1995 Colima–Jalisco (Mexico) earthquake (M_w 8), Part II: A study of the rupture process, *Geophys. Res. Lett.,* **24,** 1019–1022.

DeMets, C., Wilson, D.S., 1997. Relative motions of the Pacific, Rivera, North American, and Cocos Plates since 0.78 Ma, *J. geophys. Res.,* **102,** 2789–2806.

DeMets, C., Dixon, T., 1999. New kinematic models for Pacific-North America motion from 3 Ma to present—I: Evidence for steady motion and biases in the NUVEL-1A model, *Geophys. Res. Lett.,* **26,** 1921–1924.

Dieterich, J., 1979. Modelling of rock friction: 1. Experimental results and constitutive equations, *J. geophys. Res.,* **84,** 2161–2168.

Donnellan, A., Lyzenga, G.A., 1998. GPS observations of fault afterslip and upper crustal deformation following the Northridge earthquake, *J. geophys. Res.,* **103,** 21 285–21 297.

Dziewonski, A.M., Ekstrom, G., Salganik, M.P., 1997. Centroid-moment tensor solutions for October–December 1995, *Phys. Earth planet. Inter.,* **101,** 1–12.

Escobedo, D., Pacheco, J.F., Suárez, G., 1998. Teleseismic body-wave analysis of the 9 October, 1995 ($M_w = 8.0$), Colima–Jalisco, Mexico earthquake, and its largest foreshock and aftershock, *Geophys. Res. Lett.,* **25,** 547–550.

Ferrari, L., Pasquarè, G., Venegas, S., Castillo, D., Romero, F., 1994. Regional tectonics of western Mexico and its implications for the northern boundary of the Jalisco Block, *Geofis. Int.,* **33,** 139–151.

Ferrari, L., Rosas-Elguera, J., 2000. Late Miocene to Quaternary extension at the northern boundary of the Jalisco Block, western Mexico: The Tepic-Zacoalco Rift revised, in Cenozoic Tectonics and Volcanism of Mexico, *Geol. Soc. Am. Spec. Pap.,* **334,** 41–64.

Harris, R.A., Segall, P., 1987. Detection of a locked zone at depth on the Parkfield, California, segment of the San Andreas Fault, *J. geophys. Res.,* **92,** 7945–7962.

Heki, K., Miyazaki, S., Tsuji, H., 1997. Silent fault slip following an interplate thrust earthquake at the Japan Trench, *Nature,* **386,** 595–598.

Hudnut, K., *et al.* 1996. Coseismic displacements of the 1994 Northridge, California, earthquake, *Bull. seism. Soc. Am.,* **86,** 9–36.

Hyndman, R.D., Wang, K., 1993. Thermal constraints on the zone of major thrust earthquake failure: The Cascadia subduction zone, *J. geophys. Res.,* **98,** 2039–2060.

Klotz, J., *et al.* 1999. GPS-derived deformation of the central Andes including the 1995 Antofagasta $M_w = 8.0$ earthquake, *Pure appl. Geophys.,* **154,** 709–730.

Langbein, J., Johnson, H., 1997. Correlated errors in geodetic time series: Implications for time-dependent deformation, *J. geophys. Res.,* **102,** 591–604.

Larsen, S., 1991. Geodetic measurements of deformation in Southern California, Ph. D. thesis, California Institute of Technology.

Lundgren, P., Protti, M., Donnellan, A., Heflin, M., Hernandez, E., Jefferson, D., 1999. Seismic cycle and plate margin deformation in Costa Rica: GPS observations from 1994 to 1997, *J. geophys. Res.,* **104,** 28 915–28 926.

Mansinha, L., Smylie, D.E., 1971. The displacement fields on inclined faults, *Bull. seism. Soc. Am.,* **61,** 1433–1440.

Mao, A., Harrison, C.G.A., Dixon, T.H., 1999. Noise in GPS coordinate time series, *J. geophys. Res.,* **104,** 2797–2816.

Marone, C.J., Scholtz, C.H., Bilham, R., 1991. On the mechanics of earthquake afterslip, *J. geophys. Res.,* **96,** 8441–8452.

Melbourne, T.I., 1998. I. Rupture Properties of Large Subduction Earthquakes. II. Broadband Upper Mantle Structure of Western North America, *Ph.D thesis,* California Institute of Technology, Pasadena.

Melbourne, T., Carmichael, I., DeMets, C., Hudnut, K., Sánchez, O., Stock, J., Suárez, G., Webb, F., 1997. The geodetic signature of the M8.0 October 9, 1995, Jalisco subduction earthquake, *Geophys. Res. Lett.,* **24,** 715–718.

Mendoza, C., Hartzell, S., 1999. Fault-slip distribution of the 1995 Colima–Jalisco, Mexico, earthquake, *Bull. seism. Soc. Am.,* **89,** 1338–1344.

Menke, W., 1984. *Geophysical Data Analysis: Discrete Inverse Theory,* Academic Press, Inc., Orlando.

Okada, Y., Surface deformation due to shear and tensile faults in a half-space, 1985. *Bull. seism. Soc. Am.,* **75,** 1135–1154.

Pacheco, J.F., Sykes, L.R., Scholz, C.H., 1993. Nature of seismic coupling along simple plate boundaries of the subduction type, *J. geophys. Res.,* **98,** 14 133–14 159.

Pacheco, *et al.* 1995. The October 9, 1995 Colima–Jalisco, Mexico earthquake (M_w 8): An aftershock study and a comparison of this earthquake with those of 1932, *Geophys. Res. Lett.,* **24,** 2223–2226.

Pardo, M., Suárez, G., 1993. Steep subduction geometry of the Rivera plate beneath the Jalisco Block in western Mexico, *Geophys. Res. Lett.,* **20,** 2391–2394.

Pardo, M., Suárez, G., 1995. Shape of the subducted Rivera and Cocos plates in southern Mexico: Seismic and tectonic implications, *J. geophys. Res.,* **100,** 12 357–12 374.

Righter, K., Carmichael, I.S.E., Becker, T.A., Renne, P.R., 1995. Pliocene-Quaternary volcanism and faulting at the intersection of the Gulf of California and the Mexican Volcanic Belt, *Bull. Geol. Soc. Am.,* **107,** 612–626.

Rosas-Elguera, J., Ferrari, L., Garduno-Monroy, V.H., Urrutia-Fucugauchi, J., 1996. Continental boundaries of the Jalisco Block and their influence in the Pliocene-Quaternary kinematics of western Mexico, *Geology,* **24,** 921–924.

Ruina, A., 1983. Slip instability and state variable friction laws, *J. geophys. Res.,* **88,** 10 359–10 370.

Sandwell, D.T., Smith, W.H.F., 1997. Marine gravity anomaly from Geosat and ERS 1 satellite altimetry, *J. geophys. Res.,* **102,** 10 039–10 054.

Savage, J.C., Lisowski, M., Svarc, J.L., 1994. Postseismic deformation following the 1989 $M_w = 7.3$ Landers earthquake, southern California, *J. geophys. Res.,* **99,** 13,757–13,765.

Scholz, C.H., 1990. *The mechanics of earthquakes and faulting,* Cambridge University Press, Cambridge.

Scholz, C.H., 1998. Earthquakes and friction laws, *Nature,* **391,** 37–42.

Segall, P., Matthews, M.V., 1988. Displacement calculations from geodetic data and the testing of geophysical deformation models, *J. geophys. Res.,* **93,** 14 954–14 966.

Serpa, L., Smith, S., Katz, C., Skidmore, C., Sloan, R., Palvis, T., 1992. A geophysical investigation of the southern Jalisco Block in the state of Colima, Mexico, *Geofis. Int.,* **31,** 475–492.

Sillard, P., Altamimi, Z., Boucher, C., 1998. The ITRF96 realization and its associated velocity field, *Geophys. Res. Lett.,* **25,** 3222–3225.

Singh, S.K., Ponce, L., Nishenko, S.P., 1985. The great Jalisco, Mexico, earthquakes of 1932: Subduction of the Rivera plate, *Bull. seism. Soc. Am.,* **75,** 1301–1313.

Smith, W.H.F., Sandwell, D.T., 1997. Global sea floor topography from satellite altimetry and ship depth soundings, *Science,* **277,** 1956–1962.

Suárez, G., Sánchez, O., 1996. Shallow depth of seismogenic coupling in southern Mexico: Implications for the maximum size of earthquakes in the subduction zone, *Phys. Earth planet. Inter.,* **93,** 53–61.

Wessel, P., Smith, W.H.F., 1991. Free software helps map and display data, *EOS Trans. Am. geophys. Un,* **72,** 441–446.

Zhang, J., Bock, Y., Johnson, H., Fang, P., Williams, S., Genrich, J., Wdowinski, S., Behr, J., 1997. Southern California Permanent GPS Geodetic Array: Error analysis of daily position estimates and site velocities, *J. geophys. Res.,* **102,** 18 035–18 056.

Zumberge, J.F., Heflin, M.B., Jefferson, D.C., Watkins, M.M., Webb, F.H., 1997. Precise point positioning for the efficient and robust analysis of GPS data from large networks, *J. geophys. Res.,* **102,** 5005–5017.